LATTICE DYNAMICS OF $LaAlO_3$ AND $MgAl_2O_4$

BY

TRAVIS I. WILLETT-GIES, B.S.

A thesis submitted to the Graduate School

in partial fulfillment of the requirements

for the degree of

MASTER OF SCIENCE

Major Subject: PHYSICS

Special Concentration: SPACE PHYSICS

New Mexico State University

Las Cruces, New Mexico

May 2014

"Lattice Dynamics of LaAlO$_3$ and MgAl$_2$O$_4$," a thesis prepared by Travis Willett-Gies in partial fulfillment of the requirements for the degree, Master of Science, has been approved and accepted by the following:

Loui Reyes
Dean *ad interim* of the Graduate School

Stefan Zollner
Chair of the Examining Committee

Date

Committee in charge:

Dr. Stefan Zollner, Chair

Dr. Heinz Nakotte

Dr. Hongmei Luo

DEDICATION

I dedicate this work to my parents, Aulia Gies and Fehrunissa Willett for their eternal patience and guidance.

ACKNOWLEDGMENTS

VITA

December 27, 1990   Born in Charlottesville, VA

2008   High School Diploma from Albuquerque Academy

2010-2012   Undergraduate Assistant, Department of Physics,
                     New Mexico State University

2012   B.S. in Engineering Physics: Mechanical Concentration
                     New Mexico State University

2012-2014   Research Assistant, Department of Physics,
                     New Mexico State University

ABSTRACT

LATTICE DYNAMICS OF LaAlO$_3$ AND MgAl$_2$O$_4$

BY

TRAVIS WILLETT-GIES, B.S.

Master of Science

New Mexico State University

Las Cruces, New Mexico, 2014

Dr. Stefan Zollner, Chair

In this thesis, I present the results of Fourier-transform infrared (FTIR) ellipsometry measurements taken on two bulk aluminate materials. These high-κ metal oxides, lanthanum aluminate (LaAlO$_3$) and magnesium aluminate spinel (MgAl$_2$O$_4$), are commonly used as substrates in the semiconductor industry. By understanding the vibrational modes of these two crystalline materials, we can better predict and model the behavior of thin films grown on these substrates.

To determine the vibrational energies of these materials, we performed FTIR ellipsometry measurements over a broad energy spectrum from 250 to 8000 cm^{-1}. As atomic lattice vibrations (phonons) have the same energy as infrared (IR) photons, these vibrations will appear as peaks in the dielectric function, which is obtained directly from the ellipsometric data. The resulting spectra can be fit with a theoretical model which includes parameters of both transverse (TO) and

longitudinal optical (LO) phonons. By performing a best-fit analysis to the measured spectra, we obtain energies and broadenings for the infrared-active phonons of our chosen materials.

Using this technique, I was able to determine the parameters for all IR-active phonons within the spectral range of the ellipsometer.These parameters are reported here with unprecedented accuracy and compared with previous results obtained by IR reflectivity. The results are in agreement with theoretical density functional theory (DFT) calculations as well.

CONTENTS

LIST OF TABLES

LIST OF FIGURES

1   INTRODUCTION

High-κ dielectric materials have generated great interest in the past decade as possible replacements for silicon dioxide (SiO$_2$) as gate oxide materials in semiconductor devices. As transistors decrease in size, the thickness of the oxide must shrink proportionally. With SiO$_2$, the gate thickness is such that quantum mechanical tunneling effects begin to cause significant leakage and inefficiency in the device. Ignoring quantum effects, we can model the gate stack of a transistor as a parallel plate capacitor with capacitance given by

$$C = \frac{\kappa \epsilon_0 A}{t} \tag{1}$$

where ϵ_0 is the permittivity of free space, A is the area of the capacitor, t is the thickness of the dielectric and κ is the static dielectric constant of the material, which is defined as

$$\kappa = \epsilon(0) \tag{2}$$

The complex dielectric function $\epsilon(\omega)$ can be evaulated at zero frquency as

$$\epsilon(\omega) = \epsilon_1(\omega) + i\epsilon_2(\omega) \tag{3}$$

where ϵ_1 is related to energy stored and ϵ_2 is related to loss of energy in the material. We can see that, as A decreases proportionally to the gate dimensions, the capacitance will decrease proportionally as well. To counter this effect, either the thickness must be decreased or, as we approach the practical limits of SiO$_2$, the material should be replaced with one possessing a higher dielectric constant, κ. This inevitability of Moore's law has led to a large interest in high-κ materials in recent years.

Their implementation in practical devices is still in very early stages and we have

many aspects of the mechanisms these materials to study before they are to be considered and widely used in industry applications. In this thesis, I present my studies on atomic lattice vibrations when activated by infrared light. As electrons move through a transistor channel along the interface between Si and gate oxide, they interact with both materials and may scatter through several processes. If they collide with the nucleus of an atom in either crystalline material, they may cause it to oscillate. This absorbs energy from the electron and contributes to increased power consumption by the device. It is therefore critical to understand the energies and activity of these lattice vibrations. This knowledge is valuable not only for application in transistors but for microelectronic devices in general. $LaAlO_3$ and $MgAl_2O_4$ have excellent lattice matches with many other oxide materials such as strontium titanate ($SrTiO_3$).

1.1 Ellipsometry

I studied the phonons of $LaAlO_3$ and $MgAl_2O_4$ using Fourier-transform infrared ellipsometry. For $MgAl_2O_4$, the electronic properties were also studied using a visible to ultraviolet (VUV) ellipsometer, which measures the dielectric function in the range of electronic transitions. This was done to determine the bandgap of our sample which had been done for $LaAlO_3$ in previous work by Nelson *et al.* [1] Regardless of the wavelength, ellipsometry measures changes in polarization state and intensity of an electromagnetic wave once it interacts with a material, as shown in Fig. 1.

In practice ellipsometry uses a light source of the desired spectral region that provides unpolarized light. In the infrared, this source is a globar, which is fed into a Michelson interferometer whose moving mirror allows an entire spectrum to be taken and analyzed at once. Many scans are run to increase the signal-to-noise
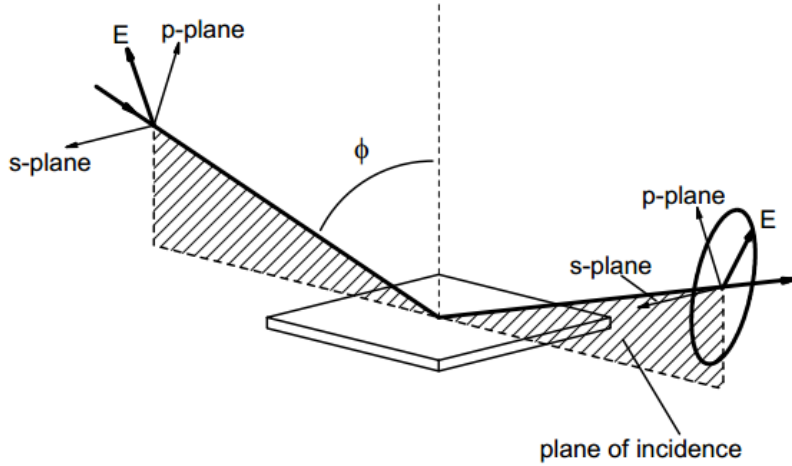
Figure 1: The principle of ellipsometry: Linearly polarized light reflected by a surface becomes elliptically polarized. Spectroscopic ellipsometry measures the change in the polarization state as a function of the wavelength. [2]

ratio and improve the data. In the visible or ultraviolet, the light from a more traditional bulb is fed into a monochromator and the measurements are performed by stepping through the wavelengths available in the source spectra. Either light source is then linearly polarized using a polarizer, which may be fixed or rotating depending on the design of the instrument. The linearly polarized light is then directed at oblique angles towards a material. As the electric and magnetic fields of the light interact with the field sources in the sample, the intensity is affected differently in the plane of the surface (s-plane) and in the plane of incidence (p-plane), which is defined by the plane containing the incident and reflected beams. By measuring the intensity ratio in each plane, r_p and r_s, using a second polarizer, the ellipsometer returns the ellipsometric angles: the amplitude ratio Ψ, and the phase differenceΔ, given by

$$\frac{r_p}{r_s} = \rho = \tan \Psi * e^{i\Delta} \tag{4}$$

We transform this information into the complex pseudodielectric function by the

equation published by Azzam and Bashara in their classic text on ellipsometry entitled *Ellipsometry and Polarized Light* [3]

$$\epsilon \approx \langle \epsilon \rangle = \left(\frac{1 - \rho^2}{1 + \rho} \right) \tan \phi^2 \sin \phi^2 + \sin \phi^2 \tag{5}$$

where ϕ is the angle of incidence and ρ is the complex reflectance ratio. This approximation is only valid for bulk isotropic samples such as the materials studied in this work. In general, the data must be modeled to determine the actual optical constants of the sample or layer in question. However, in my thesis fits were used solely to provide accurate parameters of the features being studied.

As the ellipsometer measures both Ψ and Δ, we can directly extract both the real part, $\epsilon_1(\omega)$, and imaginary part, $\epsilon_2(\omega)$, as defined in Eq. (3), from the experimental data. $\epsilon_2(\omega)$ is related to energy loss within the material so that when $\epsilon_2(\omega)$ is plotted vs. light frequency, ω, we see peaks where the light is absorbed into the medium. The data is then fit in software in an attempt to describe the various features in the spectra. In the infrared, the absorptions correspond to atomic vibrations known as phonons.

1.2 Phonons

Atoms in a crystal are held in place by the various forces of their neighbors. These include chemical bonds, Van der Waals forces or electrostatic attraction. These forces are primarily electric in nature and serve as a three dimensional potential keeping the atom in its equilibrium position. When an external electric field interacts with the positively charged nucleus of the atom, it is displaced and experiences a restoring force caused by its neighboring atoms. If, as is the case with electromagnetic radiation, the field is alternating with some frequency, the atom will oscillate with a frequency and phase determined by the external field

and the strength of its binding forces respectively. The units of this vibration are quantized, exhibit quasiparticle behavior and are known as phonons. The frequency of the atomic oscillation is equal to the frequency of the applied field. For a mathematical explanation, see appendix A.

When this approach is expanded to the entire crystal, we begin to see different types of phonons and dependencies on orientation. An acoustic phonon occurs when the entire crystal oscillates in phase with no change in average bond length. This is the method by which sound propagates through a solid and acoustic phonons can be considered to be a sound wave of arbitrarily small energy and frequency. Acoustic phonons are not visible using optical techniques. Optical phonons are oscillations within the unit cell of the crystal with the mass of the atom and strength of the bond determining the amplitude of oscillation. These phonons only occur in materials with more than one atom and they may be activated by infrared light. In an ionic bond, if the positive and negative ion oscillate opposite each other causing a time-dependent dipole moment which can couple to an external field that may be provided, for example, by the ellipsometry beam. This dipole can be along the wavevector of the external field and phonons of this type are known as longitudinal optical (LO) phonons. The alternative is for the dipole moment to be oriented perpendicular to the wave's propagation through the material and these transverse optical (TO) phonons correspond to the absorption peaks that can be resolved in an infrared optical experiment.

1.3   Models

We describe phonon contributions to the dielectric function as uncoupled harmonic oscillators using two different, but related, models. Trivially, we may describe the absorptions in the dielectric function obtained from an infrared ellip-

sometry spectrum using a set of Lorentz oscillators, the derivation of which is shown in appendix A.

$$\epsilon\left(\omega\right) = \epsilon_\infty + \sum_i \frac{A_i\omega_i^2}{\omega_i^2 - \omega^2 - i\gamma_i\omega}. \tag{6}$$

ϵ_∞ is the sum of the electronic transition contributions to the dielectric function which can be determined from visible ellipsometry, A_i is the amplitude, γ_i is the broadening and ω_i is the frequency of the ith TO phonon. Summing ϵ_∞ with the amplitudes gives a good approximation of the dielectric constant. LO phonon parameters can be extracted from this model and can be compared with those published from previous IR reflectance experiments. This is because propagation of an LO phonon in a material requires the dielectric function to be zero. By taking $\epsilon(\omega)^{-1}$, known as the loss function, poles will be found at LO frequencies. However, this model assumes the damping for LO and TO phonons can be described by a single parameter. Gervais and Piriou that this is non-physical [4].

To obtain accurate parameters for both TO and LO phonons, we must consider a factorized model including independent broadenings. Such a model can be derived from (6) and was done so by Lowndes in 1970 [5].

$$\epsilon\left(\omega\right) = \epsilon_\infty \prod_i \frac{\omega_{i,\text{LO}}^2 - \omega^2 - i\gamma_{i,\text{LO}}\omega}{\omega_{i,\text{TO}}^2 - \omega^2 - i\gamma_{i,\text{TO}}\omega} \tag{7}$$

This can easily be inverted to obtain the loss function for plotting purposes and verification of fit accuracy. It is important to note that, if $\gamma_{i,\text{TO}} = \gamma_{i,\text{LO}} = \gamma_i$, the two models are identical for a single phonon.

2   VIBRATIONAL PROPERTIES OF BULK LaAlO₃ FROM FOURIER-TRANSFORM INFRARED ELLIPSOMETRY

This article appears in Thin Solid Films as it is shown here. It is available online at `http://www.sciencedirect.com/science/article/pii/S004060901302049X` and will be published later this year in the volume covering the precedings of the 6th International Conference on Spectroscopic Ellipsometry held in Kyoto, Japan from May 26, 2013 through May 31, 2013.

Vibrational properties of bulk LaAlO₃ from Fourier-transform infrared ellipsometry

Travis Willett-Gies, Eric DeLong, Stefan Zollner
Department of Physics, New Mexico State University, MSC 3D, P.O. Box 30001, Las Cruces,
NM 88003-8001, USA

We used Fourier-transform infrared spectroscopic ellipsometry to determine the delctric function of twinned single-crystalline bulk lanthanum aluminate at 300 K in the region of lattice vibrations from 250 to 1000 cm^{-1}. We fit the experimental data using a classical sum of Lorentz oscillators as well as a factorized model. We were able to determine the parameters of five infrared-active optical phonons within our spectral range. Transverse phonons appear as peaks in the imaginary part of the dielctric function which are clearly visible without fitting. By transforming the data to obtain the loss function, we are able to observe the longitudinal phonons as peaks in the imaginary part. The polar nature of LaAlO₃ causes a strong splitting between the transverse optical (TO) and longitudinal optical (LO) phonon energies. We report energies, amplitudes and broadenings of five TO/LO phonon pairs and compare the two models used to describe the data.

2.1   Introduction

Lanthanum aluminate (LaAlO₃) is widely used as a substrate material in oxide epitaxy [6]. Recently, thin films of LaAlO₃ have drawn considerable attention

owing to the discovery of a two-dimensional electron gas in $LaAlO_3/SrTiO_3$ heterostructures [7, 8, 9]. During the early development of high-k gate dielectrics, the semiconductor industry considered $LaAlO_3$ as a replacement for SiO_2 as a gate dielectric, mostly because of its close lattice match with Si [10, 11, 12].

$LaAlO_3$ is a polar perovskite with a distorted cubic crystal structure. It can be viewed as an alternating stack of positively charged LaO and negatively charged AlO_2 planes. The distortions lead to a rhombohedral structure with space group $R\bar{3}c$ or D_{3d}^6 (space group 167) at room temperature [13, 17, 15, 16, 14]. The rhombohedral lattice constants of $LaAlO_3$ are found to be $a=b=5.365$ Å and $c=13.111$ Å using neutron powder diffraction [15, 14]. The long-wavelength optical phonon modes expected for this crystal structure are given by the factor group [17, 19, 18]

$$\Gamma\left(D_{3d}^6\right) = 2A_{1u} + 3A_{2g} + A_{1g} + 3A_{2u} + 4E_g + 5E_u. \tag{8}$$

The relationship between the cubic $Pm\bar{3}m$ or O_h^1 perovskite phonons and the crystal field splittings due to the rhombohedral distortions are summarized in Table 1 [17, 18, 19].

Near 800 K, $LaAlO_3$ transforms from the rhombohedral to the cubic crystal structure [17, 15, 14, 20]. Raman measurements of low-energy phonons with energy below 200 cm^{-1} have revealed that there is a soft phonon [17, 14] associated with this transition. The energy splitting of the lowest-energy E_g/A_{1g} phonon pair (representing the rotation of an AlO_6 octahedron) decreases with increasing temperature. At 800 K, they merge into a zero-frequency phonon with F_{2u} symmetry [17, 14].

The vibrational structure of $LaAlO_3$ has been studied both theoretically and experimentally. Abrashev et al. [19] calculated the long-wavelength optical phonon

8

frequencies using a semi-empirical shell model and plotted diagrams showing the displacement patterns of the atoms involved in the vibration. They also included the splittings between transverse (TO) and longitudinal (LO) optical phonons due to the long-range polar interactions. More recently, Delugas *et al.* [21] presented an *ab initio* density-functional and self-interaction-corrected calculation of the optical phonon frequencies, in which the TO/LO splittings were ignored. None of these calculations are sufficiently accurate for comparison with experimental results for the phonon frequencies.

The factor group analysis in Eq. (8) describes the symmetry of the optical phonons and how they can be observed experimentally. The results are summarized in Table 1: One A_{1g} mode and four E_g modes are Raman active. Three A_{2u} and five E_u modes are infrared active and can be observed with Fourier-transform infrared (FTIR) ellipsometry. Finally, two A_{1u} modes and three A_{2g} modes are silent and not accessible experimentally using first-order Raman or infrared measurements.

While most Raman spectroscopy studies have focused on the temperature dependence of the A_{1g} and E_g soft modes and their implications about the phase transition from the rhombohedral to the cubic crystal structure [17, 19, 14], the higher-energy Raman modes have also been investigated [17, 19]. Four Raman modes have clearly been identified, while the assignment of the fifth mode is controversial. See Table 1 for a summary of experimental results.

The IR-active modes have been investigated by infrared reflectance or transmittance measurements, usually followed by fitting of the dielectric function as a sum of Lorentz oscillators [18, 22, 23, 24]. Three pairs of A_{2u}/E_u modes, arising from the crystal field splitting of the three cubic $F_{1u}(\Gamma)$ modes, lead to strong features in the spectra [19]. One weak zone-folded E_u mode is also seen clearly,

9

Table 1: Summary of transverse optical phonon modes for LaAlO$_3$ at 300 K. All energies are listed in units of cm^{-1}.

R$\bar{3}$c symmetry	Pm$\bar{3}$m symmetry	activity	pattern	energy (exp)
E$_g$	F$_{2u}$(R)	Raman	AlO$_6$	33[1]
A$_{1g}$	F$_{2u}$(R)	Raman	AlO$_6$	123[2]
E$_g$	F$_{1u}$(R)	Raman	La	152[2]
E$_g$	F$_{1u}$(R)?	Raman	O	470[2] (?)
E$_g$	E$_u$(R)?	Raman	O	487[2]
A$_{2u}$	F$_{1u}$(Γ)	IR	AlO-La	188(1)[3]
A$_{2u}$	F$_{1u}$(Γ)	IR	O bend	427.0(1)[3]
A$_{2u}$	F$_{1u}$(Γ)	IR	O stretch	650.79(5)[3]
E$_u$	F$_{1u}$(Γ)	IR	AlO-La	188(1)[3]
E$_u$	F$_{2u}$(Γ)	IR	O	weak
E$_u$	F$_{1u}$(Γ)	IR	O bend	427(1)[3]
E$_u$	F$_{2g}$(R)	IR	Al	495.72(1)[3]
E$_u$	F$_{1u}$(Γ)	IR	O stretch	708.2(9)[3]
A$_{1u}$	F$_{2u}$(Γ)	silent		NA
A$_{1u}$	F$_{2g}$(R)	silent	Al	NA
A$_{2g}$	F$_{1u}$(R)	silent	La	NA
A$_{2g}$	F$_{1u}$(R)	silent	O	NA
A$_{2g}$	A$_{2u}$(R)	silent		NA

[1]Ref. [17]
[2]Ref. [19]
[3]This work using Eq. (11)

while the second E_u mode (derived from F_{2u}, which is silent in the cubic parent structure) has been considered too weak to be observable [19]. There is considerable disagreement in the literature about the exact phonon energies, amplitudes, and broadenings used to fit experimental spectra.

In this work, we determined the energies, broadenings, and amplitudes of the infrared-active optical phonons with very high accuracy using Fourier-transform infrared ellipsometry. We also describe the symmetries of all phonons and their relationships, such as rhombohedral splittings and the relationship to their cubic phonon counterparts.

2.2 Experiment and Models

Two single-side polished, 2-in. $LaAlO_3$ wafers with 0.5 mm thickness and (100) surface orientation were obtained commercially [25]. To reduce the reflections from the backside, one wafer was roughened further using a bead blaster. Our substrates are twinned and the surface orientation refers to the pseudo-cubic structure. Additional information about the samples and their properties are given in our earlier work [1], where we also report the dielectric function of $LaAlO_3$ from 0.8 to 6.6 eV between 77 and 700 K. Most importantly for the present work, our earlier research found ϵ_∞=4.12±0.01 at 300 K.

Infrared ellipsometry measurements were performed on a J.A. Woollam FTIR-VASE variable angle of incidence ellipsometer at the Center for Integrated Nanotechnologies user facility. This instrument is based on a fixed analyzer (at $0°$ and $180°$), a fixed polarizer (at $±45°$), and a rotating compensator. To increase accuracy, two fixed positions for the analyzer and polarizer were chosen (four-zone measurements), as this cancels experimental errors to first order in the analyzer and polarizer position. We measured at four angles of incidence: $60°$, $65°$, $70°$, and $75°$. Nominally, the instrument reports data between 250 and 8000 cm^{-1} but we restrict our analysis to the region of the lattice vibrations between 250 and 1000 cm^{-1}. We did not observe features in the spectra above 1000 cm^{-1} other than normal dispersion. In the spectral range around 6000 cm^{-1}, our FTIR ellipsometry results are consistent with our earlier near-IR work [1].

For various reasons, FTIR ellipsometry measurements on a bulk $LaAlO_3$ wafer are quite challenging. On the one hand, the reflectance of $LaAlO_3$ is quite low (about 11% at normal incidence in the mid-IR), much lower than for a bulk semiconductor or for a thin film on Si. In the region of the lattice vibrations,

the reflectance becomes very small [23, 26] near 300, 620, and 800 cm^{-1}. On the other hand, the phonon broadenings in LaAlO$_3$ are very low (near 4 cm^{-1} or less). We therefore select a resolution of 2 cm^{-1} for the FTIR spectrometer. These conditions create noise below 350 and near 800 cm^{-1}. We are thus forced to select a data acquisition time of eight hours to improve the signal to noise ratio, using 20 FTIR scans per spectrum and 15 spectra for each revolution of the rotating compensator.

Spectroscopic ellipsometry measures the ellipsometric angles ψ and Δ as a function of photon energy. These ellipsometric angles and the Fresnel reflectance ratio $\rho = e^{i\Delta} \tan \psi$ are related to the pseudo-refractive index $\hat{n}$ and the pseudo-dielectric function $\hat{\epsilon} = \hat{n}^2$ of the sample through [27, 28]

$$\rho = \frac{(\hat{n} \cos \phi_0 - \cos \phi_1)(\cos \phi_0 + \hat{n} \cos \phi_1)}{(\hat{n} \cos \phi_0 + \cos \phi_1)(\cos \phi_0 - \hat{n} \cos \phi_1)}, \tag{9}$$

where ϕ_0 is the angle of incidence and ϕ_1 the angle of refraction. For an ideal sample without surface overlayers, $\hat{n}$ and $\hat{\epsilon}$ are equal to the refractive index n and the dielectric function $\epsilon = n^2$. Δ equals zero or π for an ideal transparent substrate (for an insulator outside of the region of lattice vibrations), because all quantities in Eq. (9) are real. For our LaAlO$_3$ substrates, the surface overlayers are very thin (see Table I in Ref. [1]). The surface roughness is between 15 and 20 Å for our samples.

Normally, spectroscopic ellipsometry requires extensive data analysis to determine the optical constants (the complex dielectric function $\epsilon = n^2$) from the ellipsometric angles. This is not the case for our analysis. We can simply convert the measured ellipsometric angles into the dielectric function using Eq. (9), because the effect of surface roughness is negligible. The transverse optical (TO) phonons appear as peaks in the dielectric function [29, 4]. Longitudinal optical

12

(LO) vibrations are possible at energies where $\epsilon(\omega)=0$. LO phonons therefore appear as peaks in the loss function $\mathrm{Im}\,(-1/\epsilon)$.

To determine accurate phonon energies, amplitudes, and broadenings, we write the dielectric function ϵ as a function of photon energy ω as a sum of uncoupled damped harmonic oscillators [29, 4, 30]

$$\epsilon(\omega) = \epsilon_\infty + \sum_i \frac{A_i \omega_i^2}{\omega_i^2 - \omega^2 - i\gamma_i\omega}. \tag{10}$$

The first term ϵ_∞=4.12±0.01 (see Ref. [1]) describes the contributions of electronc transitions to the dielectric function. In principle, we expect eight terms in the sum, one for each infrared active phonon. In practice, some of these phonons may be very weak, while others may be degenerate. Normally, we use five oscillators as described below.

The Lorentz model (10) is derived for charges oscillating in an electric field. This model is classical and it assumes that the frictional force acting on the charge is proportional to their velocity [29]. This results in harmonic damping and a constant broadening term. (The LO broadening parameter is generally different from the TO broadening, most often larger, but not independent.)

Anharmonic coupling of phonons causes the decay of optical phonons into acoustic or other optical phonons with lower energy. Usually, the decay products are zone-edge phonons with a high density of states. If the splitting between the TO and LO phonons is large, then they will have different decay paths and their damping constants γ_{TO} and γ_{LO} may differ. Therefore, the uncoupled Lorentz oscillator model (10) often gives a good description of experimental data, which can be improved by assigning different damping parameters to LO and TO phonons

yielding [30, 31, 5, 4]

$$\epsilon\left(\omega\right) = \epsilon_\infty \prod_i \frac{\omega_{i,\text{LO}}^2 - \omega^2 - i\gamma_{i,\text{LO}}\omega}{\omega_{i,\text{TO}}^2 - \omega^2 - i\gamma_{i,\text{TO}}\omega} \tag{11}$$

as the functional form for the infrared dielectric function of insulators. If we set $\gamma_{i,\text{TO}} = \gamma_{i,\text{LO}} = \gamma_i$, then both descriptions (10) and (11) become equivalent (at least for a single oscillator or for clearly separated narrow absorption lines) [26, 31, 4].

2.3 Experimental Results

The ellipsometric angles ψ and Δ from 250 to 1000 cm^{-1} for LaAlO$_3$ at 300 K are shown in Fig. 2. Data were taken at four angles of incidence (60°, 65°, 70°, and 75°). The shape of the ψ spectra can be understood using arguments presented by Humlíček [26] for α-quartz: The first reststrahlen band with $\psi=45°$ extends from the lowest TO phonon energy at 188 cm^{-1} (below our spectral range) to the corresponding LO phonon near 280 cm^{-1}. ψ then drops to a minimum located at an energy that increases with the angle of incidence. The second restrahlen band ($\psi=45°$) extends from 427 cm^{-1} to 596 cm^{-1}. It is interrupted by a small dip at 496 cm^{-1} due to the third phonon. The energy of the second minimum also increases with the angle of incidence. The third restrahlen band has an irregular shape with contributions from two TO phonons located between 650 and 710 cm^{-1}. After the the third restrahlen band, ψ drops again. For an angle of incidence of 60°, ψ reaches zero at 1200 cm^{-1}. ψ converges to a steady state determined by ϵ_∞ near 2000 cm^{-1}. ψ never rises above 45°, which would be a sign of optical anisotropy [26]. ψ increases and decreases smoothly at the restrahlen bands (another potential sign of crystal anisotropy found in SiC) [32].

The mid-IR Brewster angle given by $\tan\phi_B = \sqrt{\epsilon_\infty}$ is 63.8°. Therefore, in the
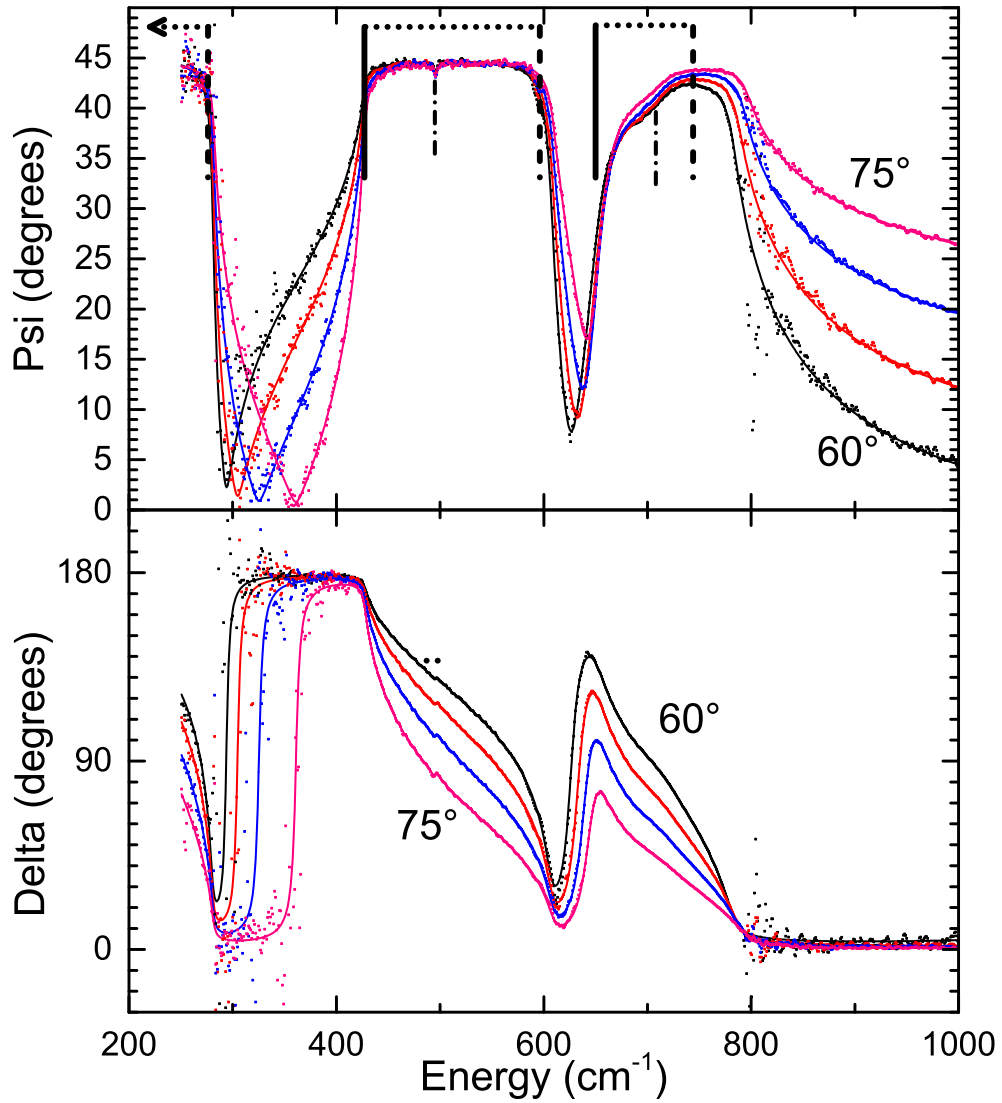
Figure 2: Ellipsometric angles ψ (top) and Δ (bottom) for LaAlO$_3$ at 300 K at four angles of incidence from 60° to 75°. Symbols: Experimental data. Lines: Fit with Eq. (11) and parameters in Table 3. Solid and dashed vertical lines indicate the location of transverse and longitudinal optical phonons, respectively.

Table 2: Transverse optical phonon mode parameters (amplitude A, TO phonon energy ω, and TO phonon broadening γ) for LaAlO$_3$ at 300 K using a Lorentz oscillator fit as in Eq. (10). 90% confidence limits for experimental results are given in parentheses. The additional parameter ϵ_∞=4.12±0.01 was fixed based on our earlier work [1].

mode	A_i (exp) (1)	ω_i (exp) cm^{-1}	γ_i (exp) cm^{-1}
AlO-La	15.24(5)	182(f)	4(f)
O bend	4.121(7)	426.94(6)	3.7(1)
Al	0.008(1)	495.8(3)	3.8(7)
O stretch	0.285(1)	652.9(1)	21.3(1)
O stretch	0.031(1)	688.6(3)	31.4(5)

Table 3: Transverse (TO) and longitudinal (LO) optical phonon energies and broadenings for LaAlO$_3$ at 300 K derived from a Lowndes oscillator fit as in Eq. (11), in units of cm^{-1}. 90% confidence limits are given in parentheses. The additional parameter ϵ_∞=4.12±0.01 was fixed based on our earlier work [1]

mode	$\omega_{i,\text{TO}}$	$\gamma_{i,\text{TO}}$	$\omega_{i,\text{LO}}$	$\gamma_{i,\text{LO}}$
AlO-La	188(1)	0.4(1)	276.4(2)	3.7(7)
O bend	427.0(1)	5.0(1)	596.1(7)	7.2(1)
Al	495.72(1)	3.8(7)	495.5(3)	3.8(7)
O stretch	650.79(5)	22.5(7)	744.1(9)	12.1(1)
O stretch	708.2(9)	55.3(9)	702.2(9)	66(1)

mid-IR, $\Delta=\pi$ for our measurements at an angle of incidence of ϕ=60°, while Δ=0 for ϕ=65° or larger. ϵ drops below 3 at 1200 cm^{-1} and thus Δ=0 between 800 and 1000 cm^{-1} for all our incidence angles. Just below the main phonon peak at 427 cm^{-1}, ϵ_1 is very large and therefore the Brewster angle is above 75°. Therefore, $\Delta = \pi$ in this range for our incidence angles (60° to 75°). ϵ_1 drops below the main phonon resonance (427 cm^{-1}) and therefore Δ drops to 0 as the Brewster angle crosses the angle of incidence. The weaker TO phonons between 495 and 710 cm^{-1} cause more gradual changes in Δ. Below 300 cm^{-1}, Δ rises again due to the influence of the TO phonon at 188 cm^{-1} (below our spectral range).

An excellent description of the ellipsometric angles can be achieved using a fit

with the Lorentz model in Eq. (10) and the parameters in Table 2. The average mean square deviation between our experimental data and the Lorentz model is only 40% larger than the experimental errors. The low-frequency dielectric constant is given by [29]

$$\epsilon_s = \epsilon_\infty + \sum_i A_i = 23.81 \pm 0.06 \tag{12}$$

using the parameters in Table 2. The dominant contribution arises from the strong TO phonons at 188 and 427 cm^{-1}. This infrared optical measurement is in excellent agreement with electrical measurements [33] at 145 GHz and with density functional calculations [21].

An even better description of our experimental data (where the mean square deviation is slighly smaller than the experimental errors) is achieved with Lowndes' model in Eq. (11) and the parameters in Table 3. At the scale in Fig. 2, it is not possible to pinpoint the improvements in the fit with the Lowndes model compared to the Lorentz oscillator model.

Therefore, we compare the dielectric functions and loss functions for both models in Figs. 3, 4, 5 and 6. As a reminder, TO phonons appear as peaks in ϵ_2 and LO phonons appear as peaks in $\text{Im}\,(-1/\epsilon)$. The Lorentz model has the following issues describing the experimental data, which are clearly improved by the Lowndes model: (1) The minimum and maximum of ϵ_1 between 600 and 700 cm^{-1} are too shallow. (2) The asymmetry of the peak in ϵ_2 at 650 cm^{-1} is not described well. See especially near 600 cm^{-1}. (3) The minima and maxima in $\text{Re}\,(-1/\epsilon)$ and the peaks in $\text{Im}\,(-1/\epsilon)$ are too shallow.

The static dieletric constant can also be calculated from Eq. (11) by setting $\omega = 0$, leading to the common Lyddane-Sachs-Teller (LST) relation for multiphonon

Figure 3: Pseudodielectric function for LaAlO₃ at 300 K calculated from the data in Fig. 2 using Eq. (9). Symbols: Experimental data. Lines: Fit with Eq. (10). Peaks corresponding to transverse optical phonons are found at 427, 496, 653, and 689 cm^{-1}.

18

Figure 4: Loss function $-1/\epsilon$ for LaAlO$_3$ at 300 K calculated from the data in Fig. 2 using Eq. (9). Symbols: Experimental data. Lines: Fit with Eq. (10). Peaks corresponding to longitudinal optical phonons are found at 277, 596, 703, and 744 cm^{-1}.

systems

$$\epsilon_0 = \epsilon_\infty \prod_i \frac{\omega_{i,\text{LO}}^2}{\omega_{i,\text{TO}}^2} = 22.3 \pm 0.3 \tag{13}$$

with parameters and errors taken from Table 3. The largest sources of error are uncertainties in the high-frequency dielectric constant ϵ_∞ and the lowest TO phonon energy (which is a fit parameter, but below our spectral range). Since the Lowndes model (11) gives a better description than the Lorentz model (10), we believe that the LST relation (13) gives a more accurate value of ϵ_0 than Eq. (12), despite the larger error bar.

Finally, we note that our data show no evidence of a weak E_u phonon peak expected at 300 cm^{-1}. Our data is very noisy at such long-wavelengths. We do not find any "ghost" peaks at other energies.

2.4 Discussion

Our infrared ellipsometry data yield very accurate phonon parameters for the Lorentz model (see Table 2) and the Lowndes model (see Table 3). We find that the Lowndes model gives a superior description of the experimental results, especially at peaks in the loss function related to LO phonons. This result is not surprising, since the main feature of the Lowndes model is the assignment of independent broadening parameters to the LO phonons, while the Lorentz model assumes that both TO and LO phonons have the same broadenings.

For isolated strong phonon modes, both models yield nearly identical TO phonon energies (compare Tables 2 and 3). However, if two TO phonon peaks overlap, then the two models find significantly differently TO phonon energies. This is true especially for the weak E_u oxygen stretch mode at 709 cm^{-1}. In general, the TO phonon energy from our model is lower than the LO phonon energy (as expected), but there is an exception for the very weak phonon located at 497

Figure 5: Pseudodielectric function for LaAlO₃ at 300 K calculated from the data in Fig. 2 using Eq. (9). Symbols: Experimental data. Lines: Fit with Eq. (11).

21

cm^{-1}, where the LO-TO separation is small and negative. In our analysis, the negative Coulomb splitting for the Al mode is only 0.2 cm^{-1}, much smaller than the resolution of our spectra (2 cm^{-1}). It is possible that a good fit to our raw data could also be found with a positive Coulomb splitting for the Al mode at 496 cm^{-1}. The weak phonon mode near 705 cm^{-1} is also inverted, but the splitting is ten times smaller than its phonon broadening. There has been some discussion in the literature about the sign of the TO/LO phonon splitting in quartz and complex metal oxides, which we did not find convincing [36, 35, 37].

Based on an argument presented by Lowndes [5] and a generalized condition for multi-phonon systes in Ref. [38], we expect that the LO broadening should be larger than the TO broadening for a material like GaAs with a single TO-LO phonon pair. This result is confirmed for most phonon modes, except for the anomalously small LO phonon broadening of the LO phonon with the largest energy. The broadenings of the two highest-energy phonons can also be found by visual inspection of ϵ_2 and $\text{Im}\,(-1/\epsilon)$ in Figs. 5 and 6. The ϵ_2 spectrum shows a sharper TO phonon at a lower energy (near 650 cm^{-1}) and a much broader TO phonon at a higher energy. Similarly, the loss function $\text{Im}\,(-1/\epsilon)$ shows a broad TO phonon at about 700 cm^{-1} accompanied by a sharper LO phonon at a higher energy. Therefore, the broadenings of the TO and LO phonons at the two highest energies are a direct experimental observation, not a numerical artifact. A comparison of our FTIR ellipsometry results with previous FTIR reflectance measurements and theoretical results is given in Table 4.

2.5 Conclusions

We have characterized the parameters of the five IR-active optical phonons of LaAlO$_3$. We were able to find the energies, amplitudes and broadenings not only of

22

Table 4: Comparison of our experimental FTIR ellipsometry results (last column) with theory and previous FTIR reflectance measurements. TO and LO phonon energies are in units of cm^{-1}. 90% confidence limits are given in parentheses.

Mode	Theory [19]	Theory [21]	Reflectance [22]	Ellipsometry (This Work)
	TO/LO	TO	TO	TO/LO
A_{2u}	213/263	168		
E_u	220/263	179	182	188(1)/276.4(2)
E_u	270/270	297		
A_{2u}	366/496	409		
E_u	371/475	411	429	427.0(1)/596.1(7)
E_u	481/505	478	501	495.72(1)/495.5(3)
A_{2u}	706/712	627	657	650.79(5)/744.1(9)
E_u	707/712	637	695	708.2(9)/702.2(9)

the reasonably well-documented TO phonons, but also of the LO phonons which have not previously been determined experimentally. Combining our Lorentz amplitudes with the ϵ_∞ previously determined by Nelson *et al.* [1], we have found an experimental dielectric constant of about 22-24. This agrees well with published values for LaAlO$_3$which range from 23 to 25 [34]. By characterizing both the TO and LO phonons, we have a more complete picture of the lattice dynamics of the material. This is vital when considering the possible applications of LaAlO$_3$in microelectronics.
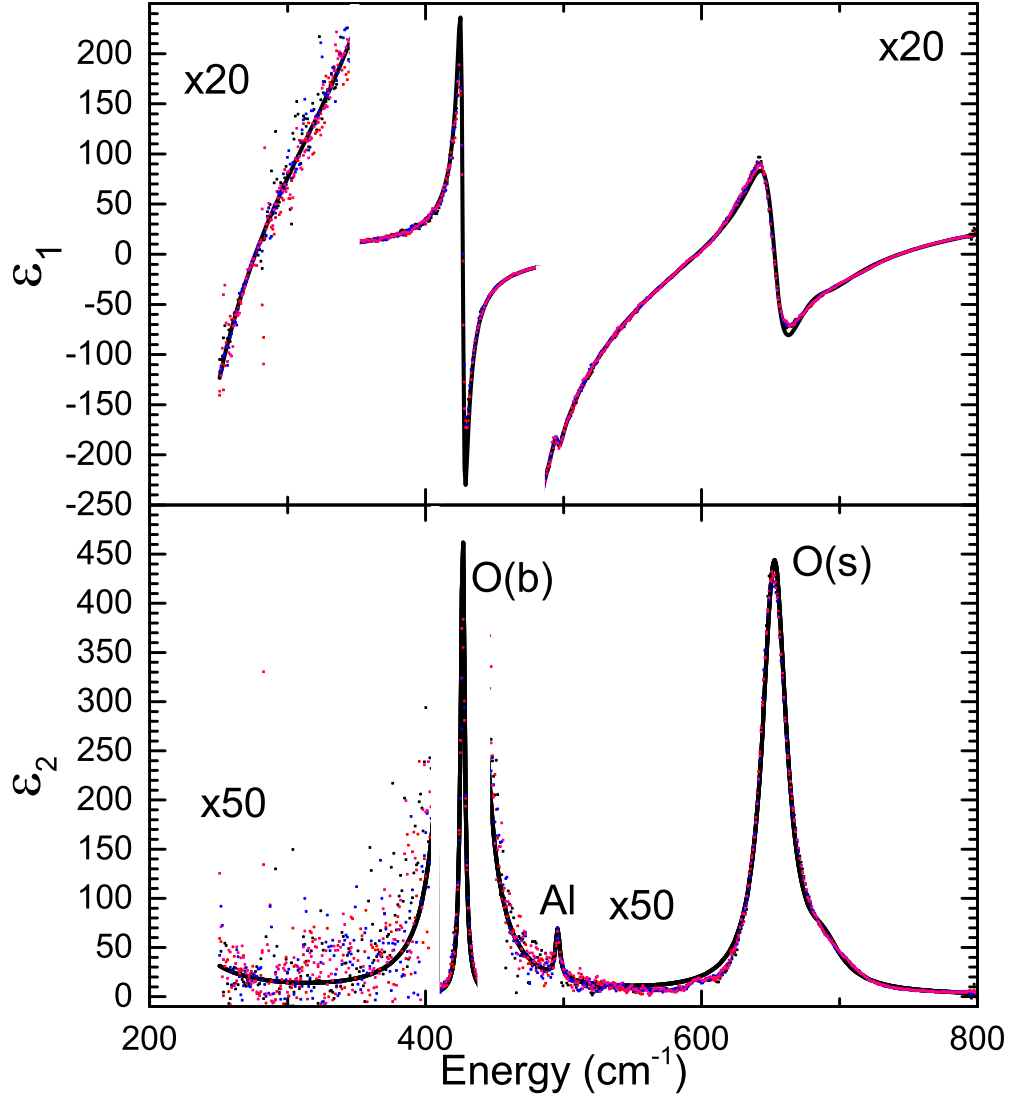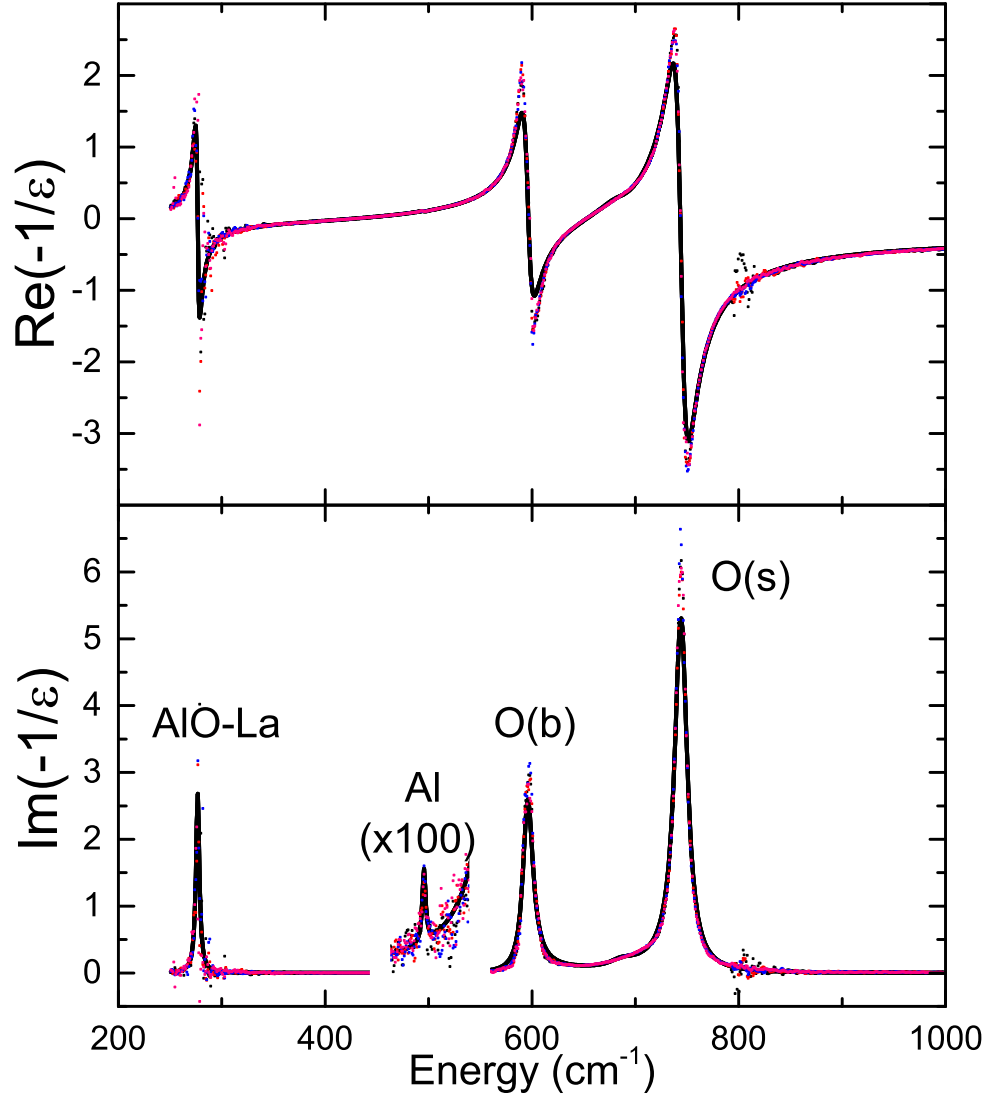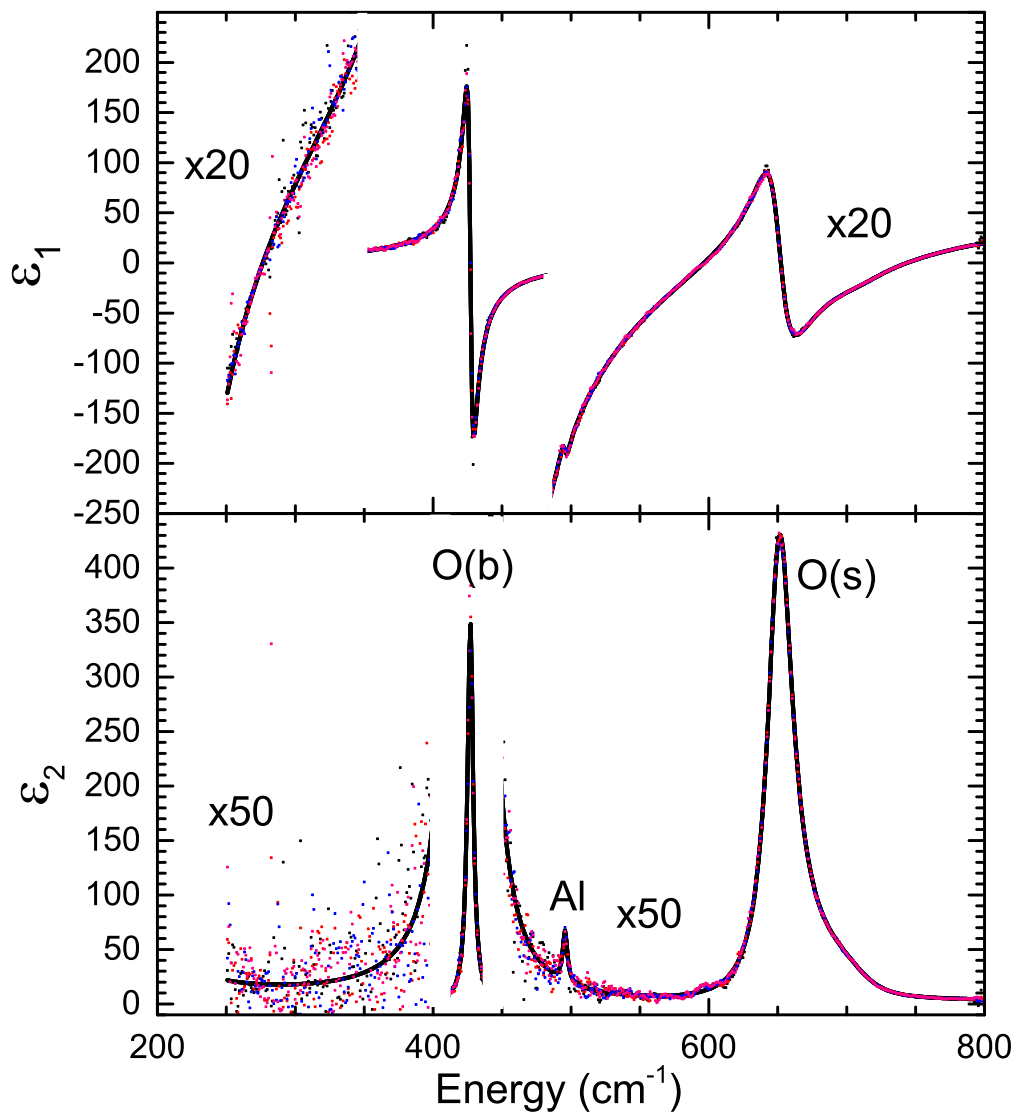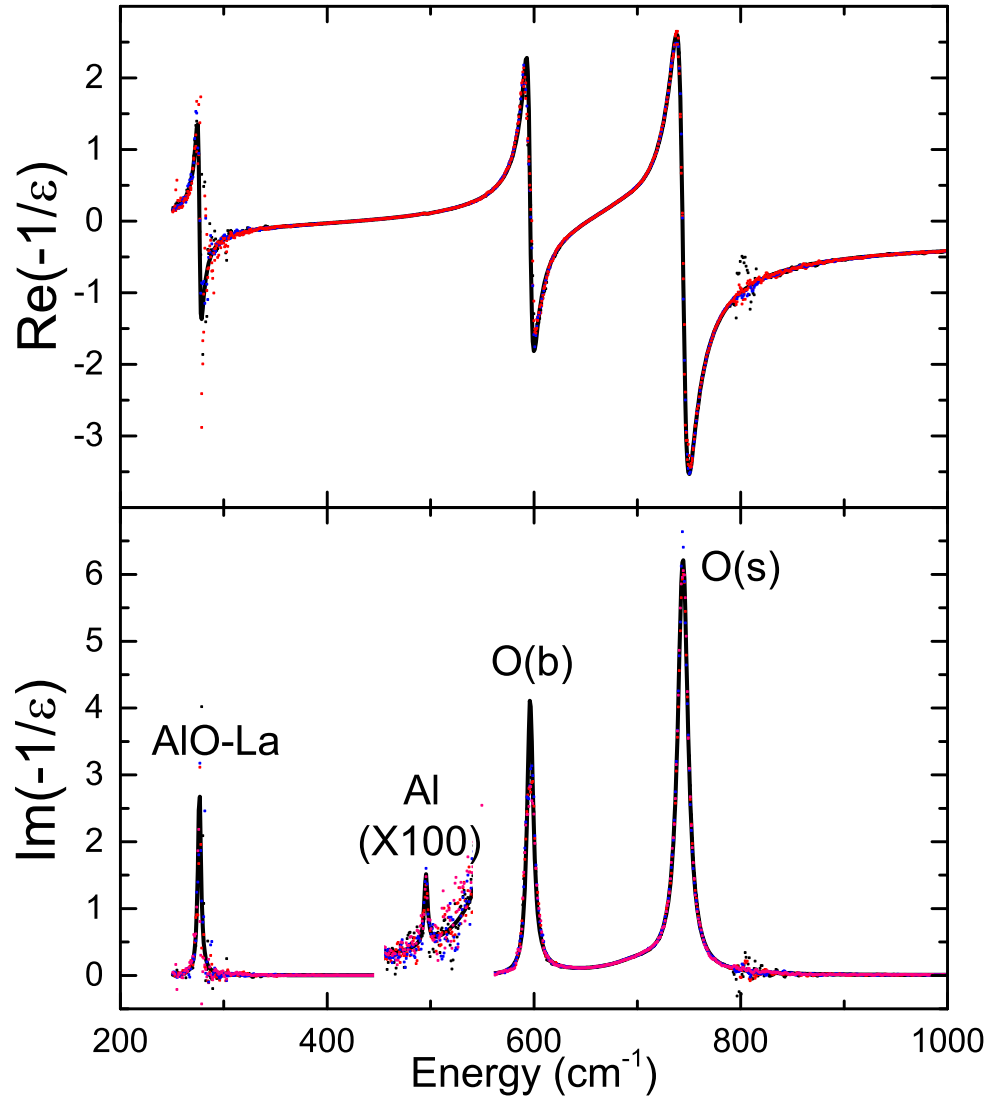
Figure 6: Loss function $-1/\epsilon$ for LaAlO$_3$ at 300 K calculated from the data in Fig. 2 using Eq. (9). Symbols: Experimental data. Lines: Fit with Eq. (11).

24

3 INFRARED TO VACUUM-ULTRAVIOLET STUDIES OF SPINEL ($MgAl_2O_4$)

This article appears in Thin Solid Films as it is shown here. It is available on-line at `http://www.sciencedirect.com/science/article/pii/S0040609013020506` and will be published later this year in the volume covering the precedings of the 6th International Conference on Spectroscopic Ellipsometry held in Kyoto, Japan from May 26, 2013 through May 31, 2013.

Infrared to Vacuum-Ultraviolet Ellipsometry Studies of Spinel ($MgAl_2O_4$)

Christian J. Zollner[1], Travis Willett-Gies[2], Stefan Zollner[2], Sukgeun Choi[3]

[1] School of Applied and Engineering Physics, Cornell University, Ithaca, NY 14853, USA

[2] Department of Physics, New Mexico State University, MSC 3D, P.O. Box 30001, Las Cruces, NM 88003-8001, USA

[3] National Renewable Energy Laboratory, Golden, CO 80401, USA

The dielectric function and the loss function for spinel ($MgAl_2O_4$) were determined using Fourier-transform infrared ellipsometry from 250 to 1000 cm^{-1}. We fit our data using two different dispersion models: (1) The Lorentz oscillator model describes the lattice optical response using a sum of independent classical harmonic oscillators with constant damping. (2) We also use a factorized oscillator model with independent broadening parameters for the transverse and longitudinal optical phonons. By fitting our data to these models, we determine the transverse and longitudinal optical phonon energies, their broadenings, and their amplitudes. The factorized model provides a better description of the data at high energies. The agreement is not so good for the lower-energy phonons, presumably due to broadenings caused by cation disorder. We also studied the Raman-active phonons by Raman spectroscopy. Using spectroscopic ellipsometry, we also determine the dispersion of the refractive index from 0.76 to 9.0 eV. Combining both data sets we find the high- and low-frequency dielectric constant. In the visible and ultraviolet region, the data are dominated by a Lorentz oscillator peak at 8.1 eV masked by surface roughness (13−16 Å).

3.1 Introduction

Magnesium aluminum spinel ($MgAl_2O_4$) is a member of a family of minerals with formulation $A^{2+}B_2^{3+}O_4^{2-}$ known as spinels. Spinel crystals (formerly known as Balas ruby) occur naturally in gemstone-bearing gravels in Sri Lanka and other areas of Asia as well as in Africa. Particularly large specimens are valued as gemstones in the crown jewels of many royal families. Spinel crystallizes in the cubic crystal system, with the oxide anions arranged in a cubic close-packed lattice and the cations Mg^{2+} and Al^{3+} occupying the octahedral and tetrahedral lattice sites, respectively. Disorder at the cation sites (Mg at Al lattice sites or vice versa) is common, especially in synthetic crystals. At high temperature and pressure, spinel decomposes into MgO and Al_2O_3 [35]. As a substrate material, it is a good alternative to sapphire for semiconductor and oxide epitaxy [39]; for example, it has an excellent thermal expansion and lattice match with GaN epitaxial films. Spinel substrates have also been used as alternatives to GaAs in InGaAs-based solar cells [40].

Spinel ($MgAl_2O_4$) belongs to the space group $Fd3m$ (O_h^7) and has two formula units (N=14 atoms) per unit cell leading to $3N - 3 = 39$ optical phonon modes with symmetry

$$\Gamma = A_{1g} + E_g + T_{1g} + 3T_{2g} + 2A_{2u} + 2E_u + 4T_{1u} + 2T_{2u}.$$

Only the four T_{1u} modes are infrared active and appear as absorption peaks in Fourier-transform infrared (FTIR) ellipsometry. The A_{1g}, E_g, and T_{2g} modes are Raman active; the remainder are silent [35].

The vibrational spectra of spinel have previously been investigated using Raman and FTIR reflectance measurements and theoretical calculations of various
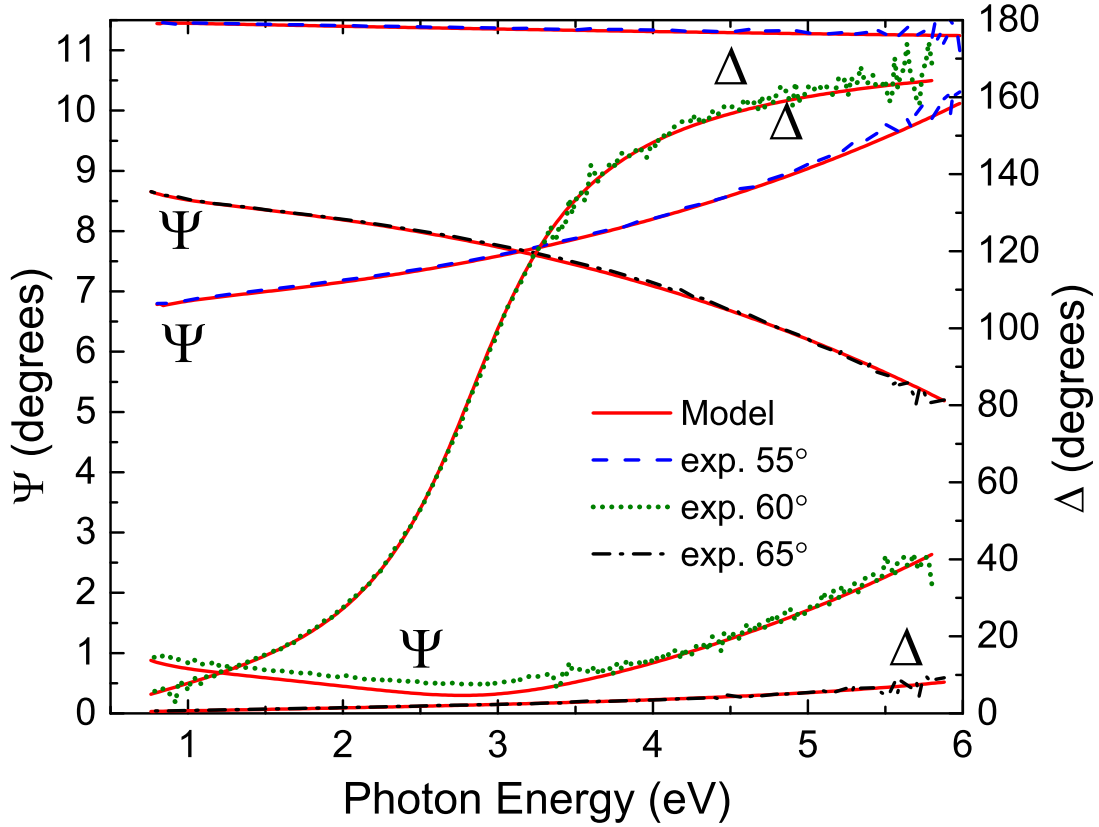
Figure 7: Ellipsometric angles ψ and Δ for spinel at incidence angles from $55°$ to $65°$ at 300 K. The solid lines show the best fit to the data using a model with two poles (IR and UV) for the spinel substrate and 13.7 Å of surface roughness.

levels of sophistication. See [35, 41] for a review. In this work, we report FTIR ellipsometry spectra of spinel, including its dielectric function and loss function. We fit these spectra using two different lattice absorption models to determine the transverse (TO) and longitudinal optical (LO) phonon energies, their amplitudes, and broadenings for all four infrared active phonons. We also report spectroscopic ellipsometry data from 0.76 to 9.0 eV and determine the dispersion of the complex refractive index in this spectral range and the high-frequency dielectric constant. Combining our FTIR and near-IR/visible/UV ellipsometry results, we determine the static dielectric constant.

Unlike reflectance and transmission measurements, ellipsometry requires no Kramers-Kronig transformation or curve fitting to obtain the complex dielectric function. Also, FTIR ellipsometry is by design a dual-beam measurement technique, since the Fresnel ratio $\rho = r_p/r_s$ is robust towards ambient gas absorption lines. The complex reflectances r_p and r_s for p- and s-polarized light are affected equally by intensity changes.

3.2 Experimental Conditions, Samples, and Models

Ellipsometry and transmission measurements from 0.76 to 6.0 eV were taken on a J.A. Woollam VASE rotating-analyzer ellipsometer with a Berek wave plate compensator, similar to our earlier work on LaAlO$_3$ [1]; measurements above 6 eV were taken on a similar nitrogen-purged VUV-VASE system.

For IR ellipsometry, we used a J.A. Woollam FTIR-VASE ellipsometer, which is based on a fixed analyzer (0°, 180°) and polarizer ($\pm 45°$) and a rotating compensator. To increase accuracy, two positions for the analyzer and polarizer were chosen (four-zone measurements), as this cancels experimental errors to first order in the analyzer and polarizer position. We measured at four incidence angles (60°, 65°, 70°, 75°) with 4 cm^{-1} resolution, much less than the observed phonon broadenings (15 cm^{-1} or larger). The instrument reports data from 250 to 8000 cm^{-1}, but we analyze only the region of lattice vibrations between 250 and 1000 cm^{-1}. We did not observe features above 1000 cm^{-1}, only normal dispersion consistent with NIR/VIS/UV-VASE measurements within the errors of both instruments. Raman spectra were acquired with 785 nm laser excitation at a power of 100 μW and a spot size of 1 μm using a Renishaw inVia Raman microscope. Results with 532 nm excitation were similar.

Spectroscopic ellipsometry measures the ellipsometric angles ψ and Δ as a

function of photon energy. These ellipsometric angles and the Fresnel reflectance ratio $\rho = e^{i\Delta} \tan \psi$ are related to the pseudo-refractive index $\hat{n}$ and the pseudo-dielectric function $\hat{\epsilon} = \hat{n}^2$ of the sample through [27, 28]

$$\rho = \frac{(\hat{n} \cos \phi_0 - \cos \phi_1)(\cos \phi_0 + \hat{n} \cos \phi_1)}{(\hat{n} \cos \phi_0 + \cos \phi_1)(\cos \phi_0 - \hat{n} \cos \phi_1)}, \tag{14}$$

where ϕ_0 is the angle of incidence and ϕ_1 the angle of refraction. For an ideal sample without surface overlayers, $\hat{n}$ and $\hat{\epsilon}$ are equal to the refractive index n and the dielectric function $\epsilon = n^2$. This is an excellent approxation for our spinel sample between 250 and 1000 cm^{-1}. Δ equals 0 or π for an ideal transparent substrate (for an insulator outside of the region of lattice vibrations), because all quantities in Eq. (14) are real.

All measurements were performed on synthetic spinel wafers (MTI Corporation, Richmond, CA). Transmission measurements were performed on double-side polished and ellipsometry measurements on single-side polished substrates. Measurements were carried out on the as-received wafers. The manufacturer specifies a root-mean square (RMS) roughness of 8 Å. The expected surface roughness layer thickness in ellipsometry data should be approximately twice this amount (16 Å). Our attempts to clean the wafers with solvents usually resulted in an increase of the deviation of Δ from 0 or π, i.e., an increase of the surface layer thickness. Some surfaces could be improved with a UV ozone preclean, which removes carbon-related contaminants [42]. As expected for a cubic system, we found the same ellipsometry results for wafers with (100) and (111) orientations. All data shown here were obtained on a (100) wafer.

Normally, spectroscopic ellipsometry requires extensive data analysis to determine the optical constants from the ellipsometric angles. This is not the case for our FTIR ellipsometry analysis. We convert the measured ellipsometric angles

Table 5: Comparison of UV and IR pole energies ω_i and amplitudes $A_i\omega_i^2$ found using spectroscopic ellipsometry with values from Ref. [43]. See Eq. (17).

	Ref. [43]		This Work	
i	$\omega_i(\text{cm}^{-1})$	$A_i\omega_i^2(\text{cm}^{-2})$	$\omega_i(\text{cm}^{-1})$	$A_i\omega_i^2(\text{cm}^{-2})$
1	100,080	18.96×10^9	98,415	18.31×10^9
2	527.18	12.234×10^5	492.00	8.522×10^5

into ϵ using Eq. (14), because the effect of surface roughness is negligible. The transverse optical (TO) phonons appear as peaks in the dielectric function [4]. Longitudinal optical (LO) vibrations are possible at energies where $\epsilon(\omega)=0$. LO phonons therefore appear as peaks in the loss function $\text{Im}(-1/\epsilon)$.

To determine phonon energies, amplitudes, and broadenings, we write ϵ as a function of photon energy ω as a sum of uncoupled damped harmonic oscillators [29, 4, 30]

$$\epsilon(\omega) = \epsilon_\infty + \sum_i \frac{A_i\omega_i^2}{\omega_i^2 - \omega^2 - i\gamma_i\omega}. \tag{15}$$

The first term $\epsilon_\infty=2.90$ (see [41] and below) describes the contributions of electronic transitions to the infrared dielectric function. In principle, we expect four terms in this sum, one for each infrared active T_{1u} phonon. We also observe an overtone (two-phonon absorption process) near 800 cm^{-1} [35].

The Lorentz model (15) is derived for classical charges oscillating in an electric field, assuming that the frictional force acting on a charge is proportional to its velocity [29]. This results in harmonic damping and a constant broadening term. This model can be improved by assigning different damping parameters to LO and TO phonons yielding [30, 31, 5, 4]

$$\epsilon(\omega) = \epsilon_\infty \prod_i \frac{\omega_{i,\text{LO}}^2 - \omega^2 - i\gamma_{i,\text{LO}}\omega}{\omega_{i,\text{TO}}^2 - \omega^2 - i\gamma_{i,\text{TO}}\omega} \tag{16}$$

as the functional form for the infrared dielectric function of insulators. If we
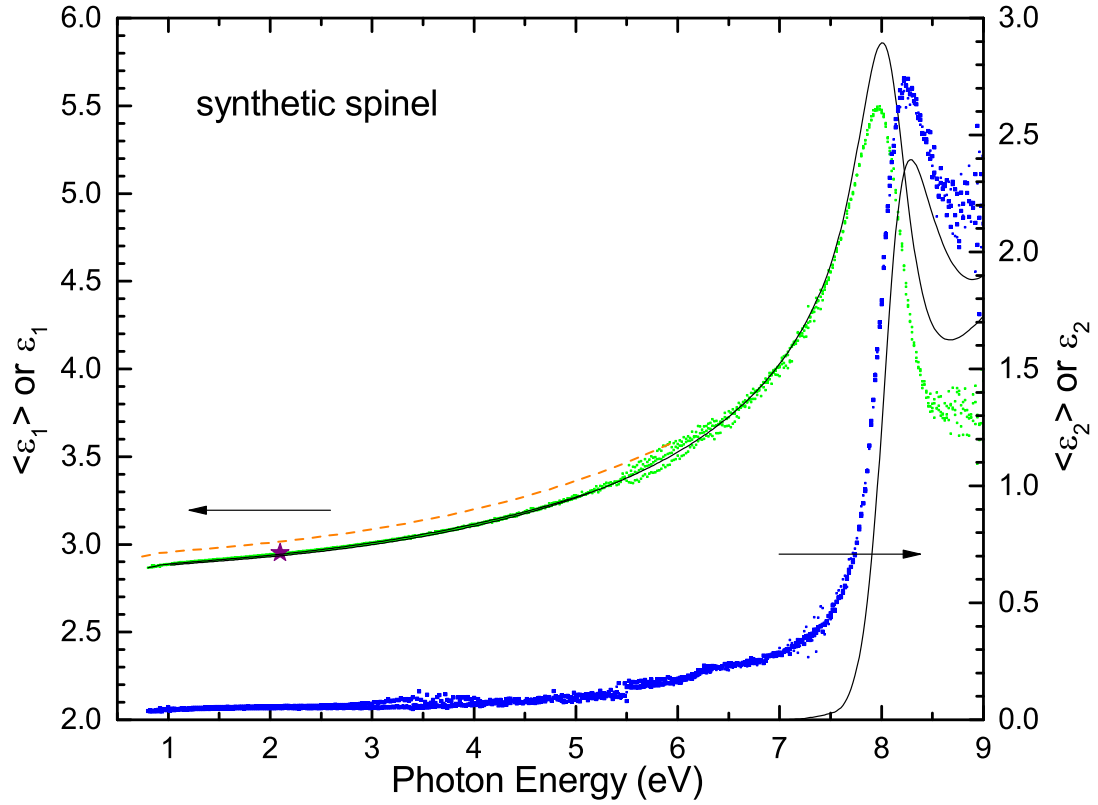
Figure 8: Symbols: Real and imaginary parts of the pseudodielectric function $\langle\epsilon\rangle$ measured at $55°$ and $65°$ angle of incidence. Data from two instruments (IR/VIS/UV and VUV) were merged at 5.5 eV. Star: Data from Ref. [44]. Lines: Solid: Dielectric function ϵ determined by roughness correction of $\langle\epsilon\rangle$. Dashed: Sellmeier model (17) based on poles in UV and IR from Ref. [43].

set $\gamma_{i,\text{TO}} = \gamma_{i,\text{LO}} = \gamma_i$, then both descriptions (10) and (16) become equivalent (at least for a single oscillator or for clearly separated narrow absorption lines) [26, 31, 4].

3.3 Experimental Results

The ellipsometric angles from 0.76 to 6.0 eV are shown in Fig. 7 at three different angles of incidence near the Brewster angle, where the measurement is most accurate. Δ switches from 0 to π for an incidence angle of 60°. The Brewster angle crosses 60° near 2.8 eV, where Δ=90°. The abruptness of this cross-over is determined by the thickness of the surface layer—data for samples with a thicker roughness layer (not shown) exhibited a broader cross-over. ψ is small (below 1°) and noisy (due to measurement errors) near the Brewster angle.

The transmission of the substrate (not shown) is above 80% below 6 eV and then drops to 60% at 6.6 eV. We conclude that the band gap of spinel is larger than 6 eV and that the material is transparent at lower photon energies. Therefore, we model the ellipsometric angles with a transparent substrate with surface roughness. The dispersion of spinel below 6 eV is described with two poles (Lorentz oscillators with zero broadenings), one of them in the UV at 12.2 eV, the other in the IR at 0.06 eV (the location of the strongest TO phonon). These values are compared with the literature in Table 5. With two poles, the Lorentz oscillator model becomes the Sellmeier equation [43]

$$\epsilon - 1 = \sum_{i=1}^{2} \frac{A_i \omega_i^2}{\omega_i^2 - \omega^2} = \frac{18.31 \times 10^9}{(98,415)^2 - \omega^2} + \frac{8.522 \times 10^5}{(492.00)^2 - \omega^2} \tag{17}$$

where ω is in cm^{-1}. Excellent agreement between model and data (see Figure 7) can be achieved up to about 6 eV with a surface roughness of 13.7 Å. As shown in Fig. 8, there is a difference between our model based on experimental

data, and that of Ref. [43] of 0.064 or 2.2% at 1 eV. Since the model in the literature is based on tabulated data from unpublished experiments, we cannot explain the discrepancy. However, the dielectric function at 2.1 eV determined from minimum deviation prism measurements by Vedam $et.$ $al.$ [44] is much closer to our ellipsometric results than to the data from Ref. [43].

The resulting dispersion up to 6 eV is shown in Fig. 8. To determine the high-frequency dielectric constant ϵ_∞, we set the amplitude for the IR pole (lattice contribution) to zero and then extrapolate the dispersion to zero photon energy (from the remaining UV pole). We obtain ϵ_∞=2.90, which agrees well with previous experimental and density-functional results [41].

Temperature-dependent measurements were taken in a liquid-nitrogen cooled vacuum cryostat from 77 to 800 K at a fixed photon energy of 2 eV. We find $d\epsilon_1/dT$=3.2$\times 10^{-5}$/K, in agreement with Vedam's value [44]. The temperature-dependence of ϵ for a crystal has two contributions: one negative contribution from the thermal expansion, and one positive contribution from the negative temperature-dependence of the band gap [45]. Both are similar in magnitude and cancel partially. Upon comparison with LaAlO$_3$ [1], whose temperature-dependent ϵ data show first a negative trend at low temperatures (where the negative thermal expansion term dominates) and then a positive trend at higher temperatures (where the band gap contribution dominates), spinel exhibits no downward-sloping region.

Figure 8 also shows $\langle\epsilon\rangle$ up to 9 eV. Above 6 eV, Eqn. (17) is no longer suitable to describe ϵ because of the presence of an excitonic interband transition at 8.1 eV. Instead, a Tauc-Lorentz oscillator and one Gaussian peak were used to model our data. Since the surface roughness was determined from the data at lower energies, $\langle\epsilon\rangle$ (symbols) can be corrected to estimate ϵ (lines) up to 9 eV. Surface roughness
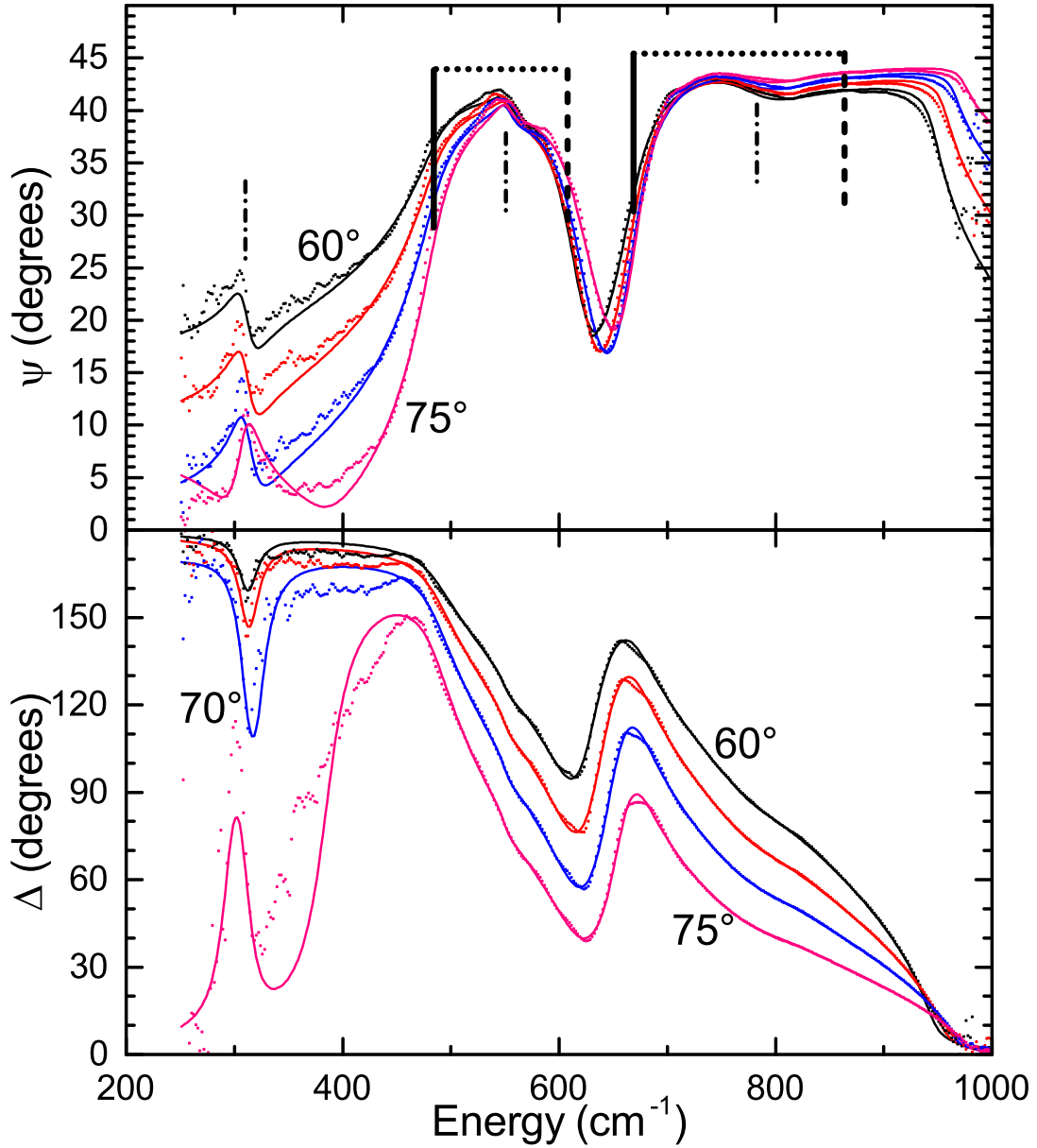
Figure 9: Ellipsometric angles ψ (top) and Δ (bottom) for $MgAl_2O_4$ at 300 K at four angles of incidence from 60° to 75°. Symbols: Experimental data. Lines: Fit with the Lowndes model given in Eq. (16) and parameters in Table 7. Solid and dashed lines show the location of TO and LO phonons respectively; dot-dashed lines show TO and LO phonons that are nearly degenerate.

Table 6: Transverse optical phonon mode parameters (amplitude A, TO phonon energy ω, and TO phonon broadening γ) for $MgAl_2O_4$ at 300 K using a Lorentz oscillator fit as in Eq. (10). 90% confidence limits for experimental results are given in parentheses. The additional parameter ϵ_∞=2.90 was fixed based on measurements in the visible spectrum. Results from Ref. [35] are given for comparison. The mode in the last row is likely to be an overtone.

mode	A_i (1)	ω_i cm^{-1}	γ_i cm^{-1}	A_i [35] (1)	ω_i [35] cm^{-1}	γ_i [35] cm^{-1}
T_{1u}	0.4(f)	307.3(5)	15(f)	0.28	307.3	5.0
T_{1u}	4.03(7)	481.7(1)	35(f)	4.2	476.5	13.0
T_{1u}	0.03(f)	570(f)	20(f)	0.065	577.8	12.0
T_{1u}	0.61(4)	665(1)	30(f)	0.8	676.2	30.5
?	0.005(f)	800(f)	50(f)	0.06	808.5	50

decreases the peak of $\langle\epsilon_1\rangle$ and increases the peak of $\langle\epsilon_2\rangle$, similar to the E_1 peak of Si. Our ϵ_2 peak at 8.1 eV is much stronger than the peak found in [46]. Aboe 8.5 eV, ϵ_2 rises again consistent with [46].

FTIR ellipsometry data for bulk spinel, represented by ellipsometric angles, are shown in Fig. 9 at four angles of incidence. ψ shows a peak near 310 cm^{-1} from a nearly degenerate TO/LO phonon pair and *reststrahlen* bands from 480 to 610 cm^{-1} and from 670 to 950 cm^{-1} due to strong TO/LO phonon pairs with significant Coulomb splittings. These bands do not have flat tops, but are interrupted by dips near 550 and 800 cm^{-1} due to weak TO/LO phonon pairs with smaller splittings.

We fit the ellipsometric angles using an expression for ϵ as shown in Eq. (15) with parameters given in Table 6. Our results are comparable to those of Ref. [35], but differences exist. Most notably, the phonon broadenings are about twice as large for our synthetic crystal than for the natural crystal measured in Ref. [35]. The largest differences between data and model are found in the shoulders of the TO peaks, presumably an indication of cation disorder [35]. Adding the contributions of electronic transitions and the four IR-active TO modes to the

Table 7: Transverse (TO) and longitudinal (LO) optical phonon energies and broadenings for $MgAl_2O_4$ at 300 K derived from a Lowndes oscillator fit as in Eq. (16), in units of cm^{-1}. 90% confidence limits are given in parentheses. The additional parameter ϵ_∞=2.90 was fixed based on work in the visible spectrum. The mode in the last row is likely to be an overtone.

mode	$\omega_{i,\mathrm{TO}}$	$\gamma_{i,\mathrm{TO}}$	$\omega_{i,\mathrm{LO}}$	$\gamma_{i,\mathrm{LO}}$
T_{1u}	307.5(9)	18(1)	312.5(9)	22(1)
T_{1u}	484.4(8)	36.3(5)	608.8(9)	43.3(5)
T_{1u}	551.4(4)	21.0(9)	552.5(8)	18.9(8)
T_{1u}	669.6(1)	37.0(6)	864.8(1)	31.7(2)
Other	783.8(6)	95.7(1)	779.8(2)	73.7(0)

Table 8: Comparison of experimental phonon energies found using spectroscopic ellipsometry with theoretical values found using density functional theory (DFT) and experimental values from FTIR reflectance measurements.

DFT	Reflectance (Ref. [41])	Reflectance (Ref. [35])	Ellipsometry (This Work)
		TO/LO (cm^{-1})	
307/309	303/307	304/312	307.5(9)/312.5(9)
478/612	491/608	485/610	484.4(8)/608.8(9)
565/564	532/532	578/575	551.4(4)/552.5(8)
666/854	675/870	676/868	669.6(1)/864.8(1)
	805/796	~800	783.8(6)/779.8(2)
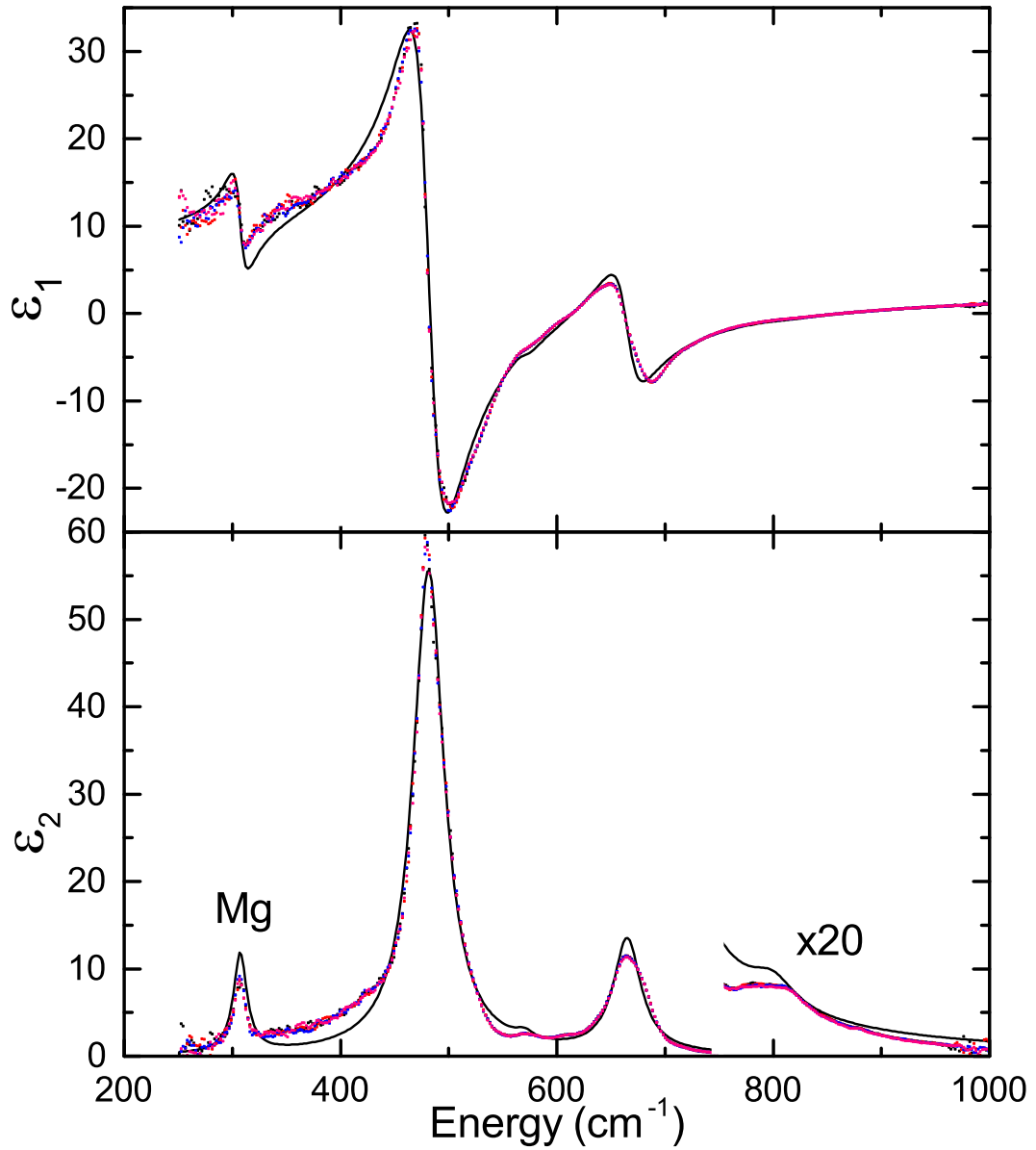
Figure 10: Pseudodielectric function for $MgAl_2O_4$ at 300 K calculated from the data in Fig. 9 using Eq. (14). Symbols: Experimental data. Lines: Fit with the Lorentz model given in Eq. (15). Peaks corresponding to transverse optical phonons are found at 307, 484, 551, and 669, cm^{-1}. An overtone appears at 783 cm^{-1}.

static dielectric constant, we find

$$\epsilon_s = \epsilon_\infty + \sum_i A_i = 8.0 \pm 0.2 \tag{18}$$

using the parameters in Table 2. The dominant contribution arises from the strong TO phonons at 482 and 665 cm^{-1}. The largest source of error (estimated to be 0.1) is in the strength of the 307 cm^{-1} mode, which is influenced by the low-energy shoulder of the 482 cm^{-1} phonon. This infrared optical measurement of ϵ_s is in excellent agreement with electrical measurements [47] at 1 MHz and density-functional calculations [41]. The dielectric and loss function determined from our experimental data and from the fit are shown in Figs. 10 and 11.

An even better description of our data is achieved with Lowndes' model in Eq. (16) and the parameters in Table 7. Our parameters are similar to those of [41], except that our broadenings might be a little smaller. The magnitude of the broadenings has been associated with cation disorder and with surface damage due to polishing of synthetic crystals. This model results in the ellipsometric angles shown by the solid lines in Fig. 9 and the dielectric and loss functions shown in Figs. 12 and 14. By setting the frequency in Eq. (16) to zero, we acquire the Lyddane-Sachs-Teller relation [48] in the form

$$\epsilon_s = \epsilon_\infty \prod_i \frac{\omega_{i,\mathrm{LO}}^2}{\omega_{i,\mathrm{TO}}^2} = 7.8 \pm 0.2 \tag{19}$$

using the parameters in Table 7.

3.4 Discussion

When we compare the dielectric and loss functions predicted by the Lorentz and Lowndes models (see Figs. 10-14), we find that both models struggle with fitting the data at low energies. Especially, they fail to predict the low-energy
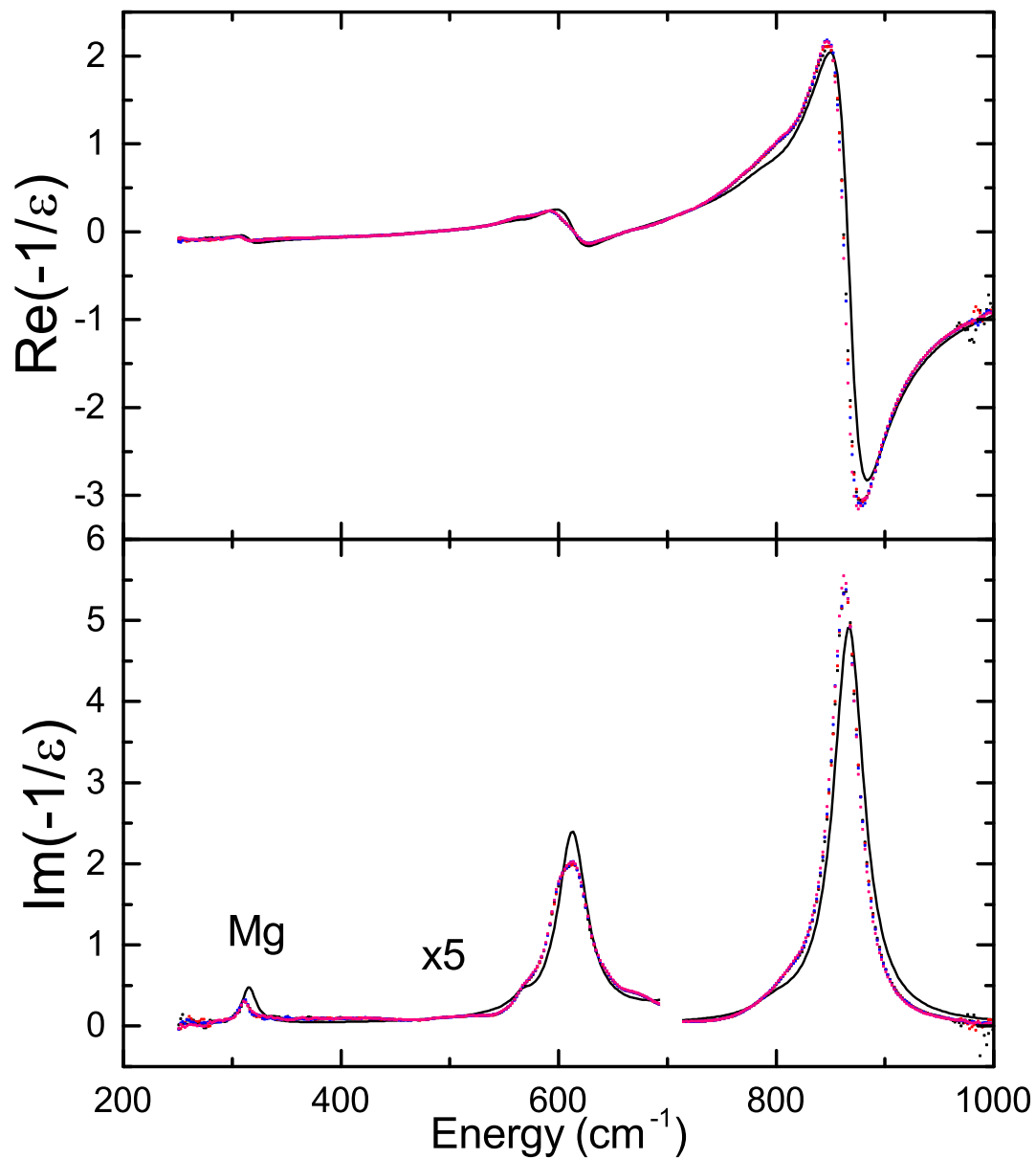
Figure 11: Loss function $-1/\epsilon$ for MgAl$_2$O$_4$ at 300 K calculated from the data in Fig. 9 using Eq. (14). Symbols: Experimental data. Lines: Fit with the Lorentz model given in Eq. (15). Peaks corresponding to longitudinal optical phonons are found at 312, 609, 558, and 864 cm^{-1}. An overtone is visible at 780 cm^{-1}.

39
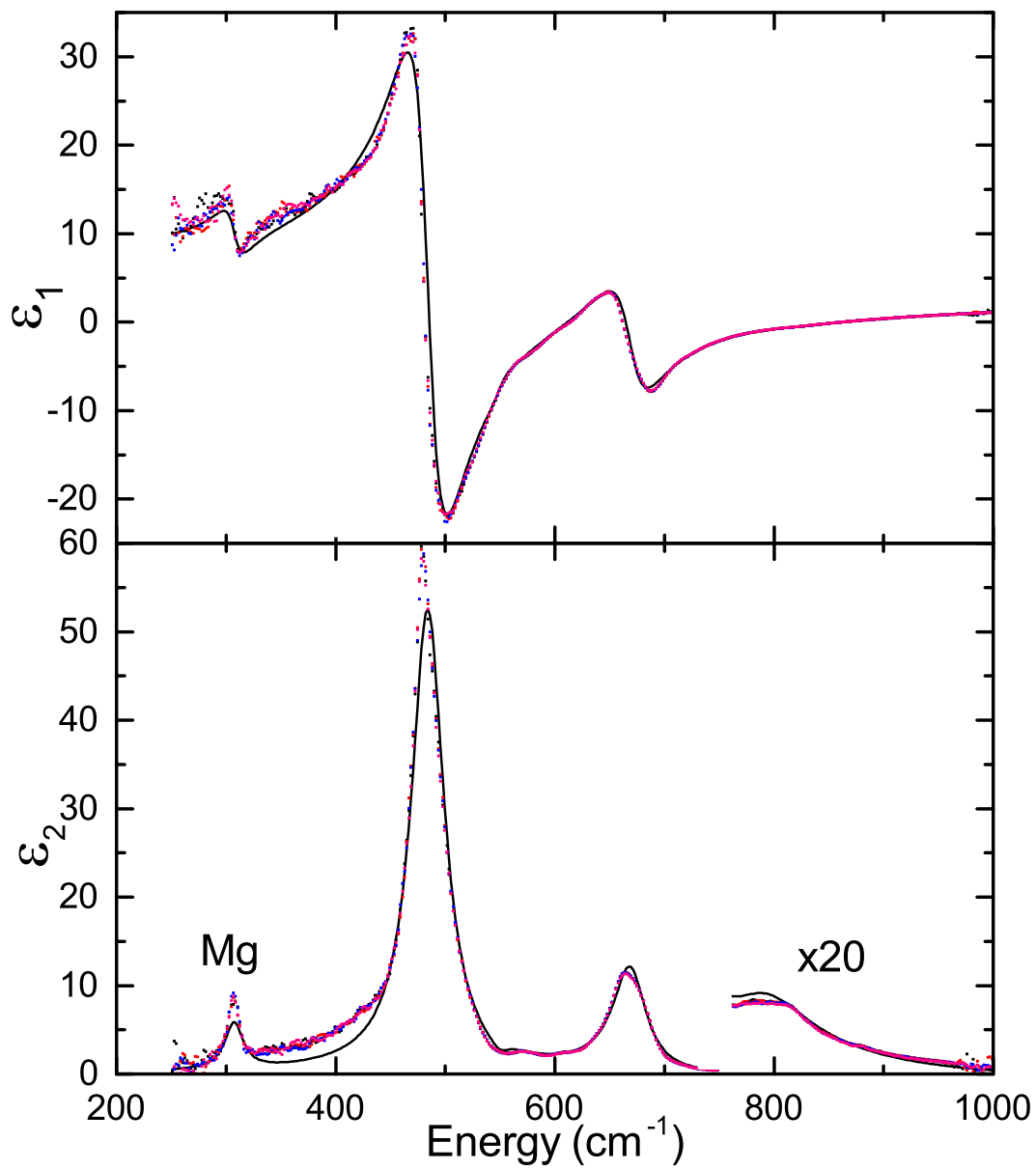
Figure 12: As Fig. 10, but fitted with the Lowndes model in Eq. (16).

shoulder of the 484 cm^{-1} TO peak assigned to cation disorder. This shoulder broadens the 308 and 484 cm^{-1} peaks and causes a poor fit. At higher energies, the Lowndes model fits the data perfectly, especially for the 670/865 cm^{-1} TO/LO pair. The fit of this mode is much worse for the Lorentz model. As for a similar study on LaAlO$_3$ [49], we conclude that the factorized Lowndes model gives a better description of FTIR ellipsometry data of insulating oxides with multiple overlapping phonon modes.

All TO-LO Coulomb splittings found using a Lowndes fit to our data are positive. In general, the weaker phonon modes have smaller TO-LO phonon splittings [36]. Ref. [41] finds a vanishing splitting of the TO/LO mode at 532 cm^{-1} (near 552 cm^{-1} in our work). By contrast, in Ref. [35] it was found that one TO/LO mode was inverted and had a negative Coulomb shift. Ref. [35] cites a mathemetical rule of Scott and Porto [36] that an LO peak must occur at a frequency between every pair of TO's for a given symmetry. Such reversals have been predicted for quartz [36] and observed for LaAlO$_3$ [49] and previous studies of spinel [35], but not in this work. There is no LO peak in our data between the T_{1u} TO peaks at 484.4 and 551.4 cm^{-1}. Mathematically, it has been stipulated [36] that one should expect to find an ϵ_1 zero (an LO mode) between two ϵ_2 peaks (TO modes), at least if the broadening is very small and both TO peaks have similar amplitudes. On the other hand, if a weak TO mode resides on the shoulder of a much stronger broad peak (as for spinel or LaAlO$_3$), it is less clear that the LO mode needs to be inverted. We are unable to answer this question experimentally with confidence, because the observed TO/LO splitting of the 552 cm^{-1} mode is only 1 cm^{-1}, while the resolution of our FTIR spectrometer is only 4 cm^{-1}.

We are not aware of calculations showing the atomic displacements for the four TO phonon modes. The lowest-energy TO mode at 307.5 cm^{-1} is usually

associated with vibrations of the Mg atom. The two strong peaks at 484 and 670 cm^{-1} have been attributed to internal vibrations of the AlO$_4$ tetrahedra and labelled ν_3 (670 cm^{-1}) and ν_4 (484 cm^{-1}). The weak mode at 551 cm^{-1} should be a combination of ν_3 and ν_4 [35].

To complement FTIR ellipsometry, we also performed Raman measurements of the same crystals, see Fig. 13. Our results are consistent with [35, 50]. We observe four of five expected Raman-active phonons and one additional peak assigned to cation disorder, which is typical for synthetic spinel crystals. This additional peak is due to a silent mode in the perfect crystal, which becomes Raman active in the disordered structure because of the coupling with the Mg tetrahedral breathing mode at 770 cm^{-1} [50].

3.5   Conclusions

The lattice dynamics of MgAl$_2$O$_4$ was investigated using FTIR ellipsometry and Raman spectroscopy. The phonon parameters (energies, broadenings, amplitudes) for all four IR-active optical phonons and one overtone were determined with high accuracy, first by identifying peaks in the dielectric function and the loss function, then by fitting the dielectric function using oscillator dispersion models. A factorized phonon model due to Lowndes describes the data better than the classical Lorentz harmonic oscillator model. All our Coulomb TO/LO phonon spilttings were found to be positive. Asymmetric broadenings of low-energy phonon peaks are explained by cation disorder. We also determined the low- and high-frequency dielectric constants by combining our infrared measurements with spectroscopic ellipsometry measurements from 0.76 to 9.0 eV. The latter measurements also yield the dispersion of the refractive index up to 9.0 eV.
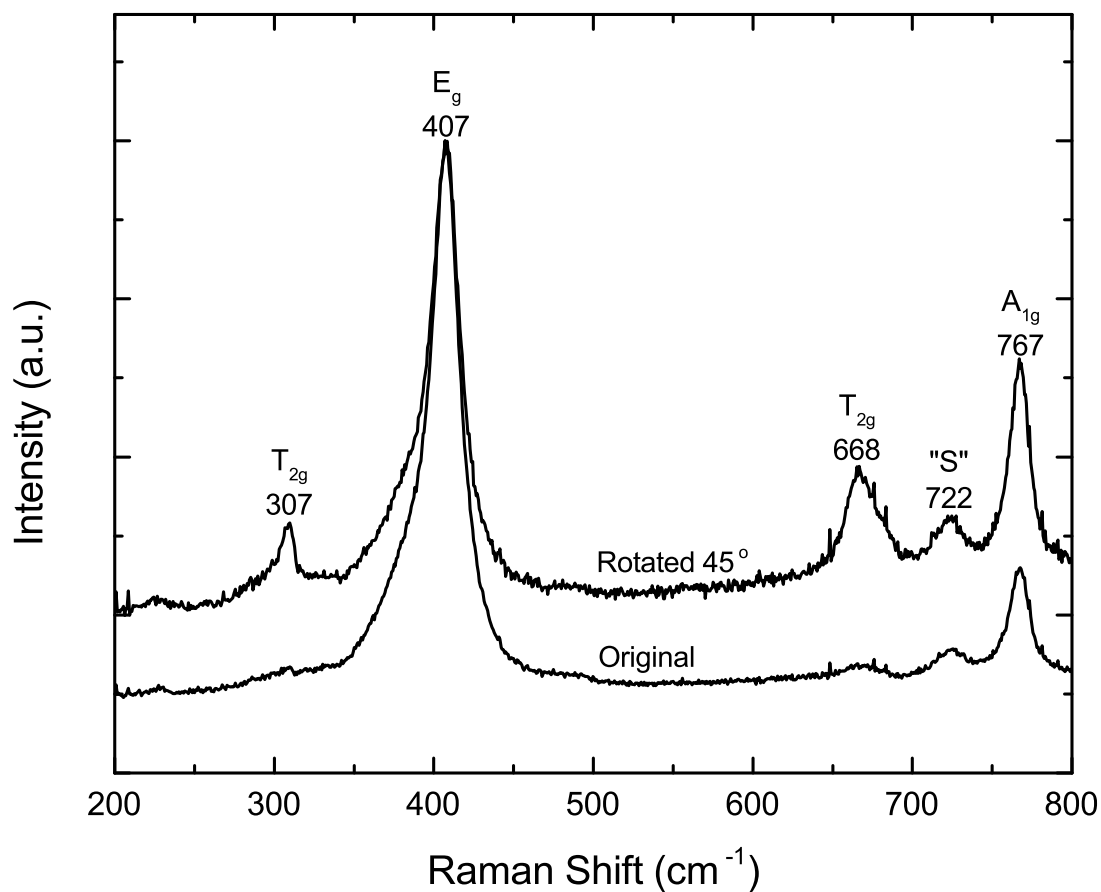
Figure 13: Raman spectra of synthetic spinel with (001) surface orientation under 785 nm excitation, normalized to the E_g maximum. The sample was rotated by 45° between the two measurements. Two T_{2g}, one E_g, and one A_{1g} mode are clearly observed. The amplitudes of the T_{2g} modes are very sensitive to sample rotation for the (001) surface, not so much for a (111) surface. The mode marked "S" is believed to be disorder-activated, since it is only observed in synthetic spinel. Peak positions in cm^{-1} are indicated.
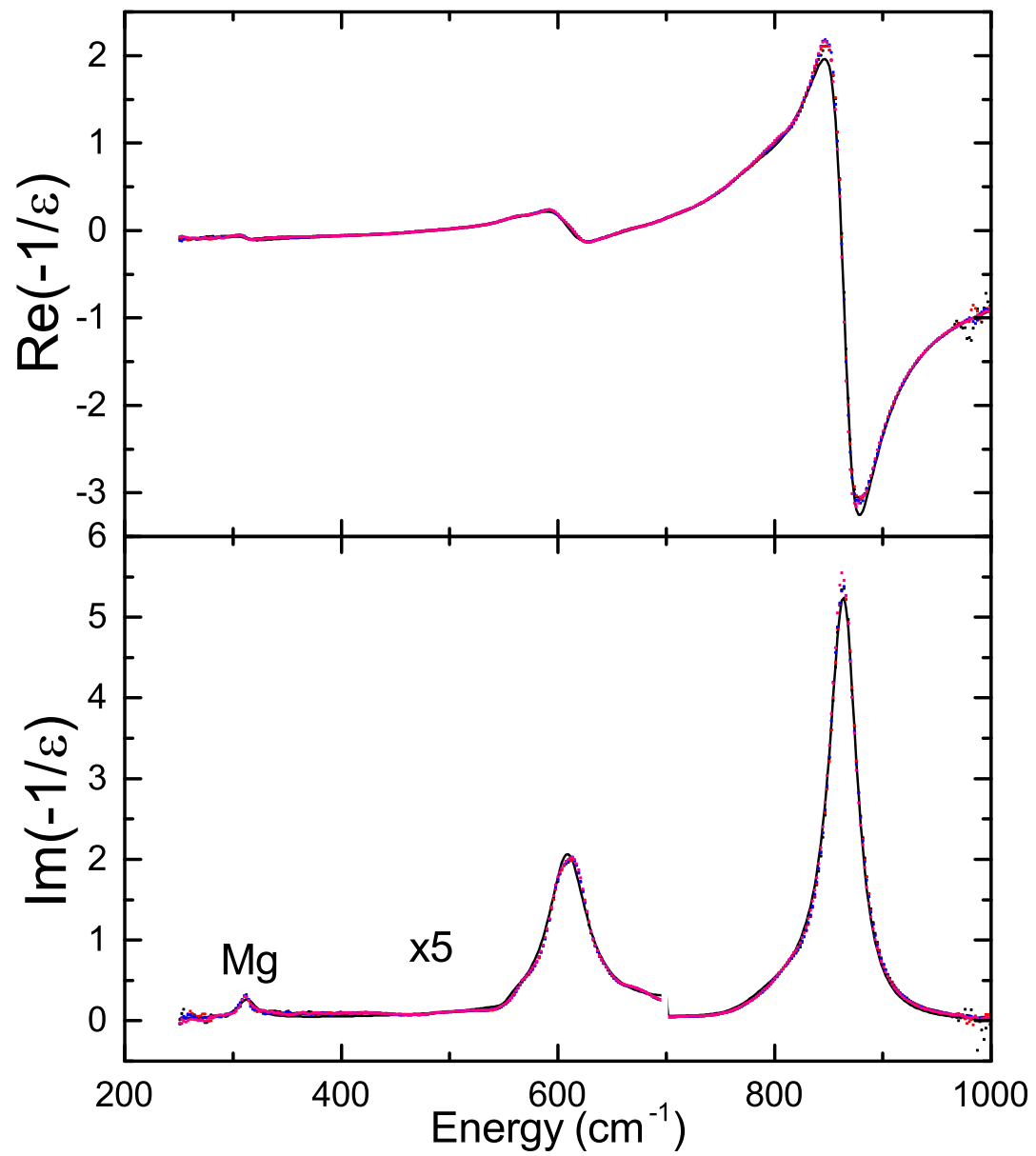
Figure 14: As Fig. 11, but fitted with the Lowndes model in Eq. (11).

4 DISCUSSION

In the two studies we have published, we have thoroughly analyzed the dielectric functions of both $LaAlO_3$ and$MgAl_2O_4$. We have accurately modeled the infrared regime for both materials using the classic sum of Lorentz oscillators and can report values for the static and high-frequency dielectric constants. We have also found the energies and lifetime broadenings of all IR active TO and LO phonons for both materials. We can compare these with previous values found using IR reflectance as well as theoretical values which continue to be calculated using increasingly accurate density functional theory (DFT). Dr. Alex Demkov and Kurt Fredrickson at the Univeristy of Texas at Austin have performed DFT within the local density approximation (LDA) for $LaAlO_3$ and we are in the process of compiling the results for comparison with our experimental phonon parameters. Difficulties arise due to the fact that both the Lorentz and Lowndes models used to describe the experimental data are derived for cubic systems. When the symmetry is lowered as is the case with $LaAlO_3$ we find that a triply degenerate mode splits into a singlet and a doublet as described in appendix B. The DFT-LDA calculations give these modes with mixed TO/LO behavior. This has led to much discussion as to the activity and assignment of the modes in our respective work.

Theoretical confusion notwithstanding, by obtaining an accurate model of the dielectric function for $LaAlO_3$ and $MgAl_2O_4$ we can improve measurements of thin films and structures grown on these common substrates. This becomes more important as device scale shrinks and design parameters grow more sensitive to substrate and interface effects. A common pursuit in materials science is to obtain a comprehensive library of possible materials to use when analyzing new or com-

plex samples. By combining the optical parameters for the entire spectral range as was done for spinel, we have an accurate model for the substrate from 137 nm to 40,000 nm. The ellipsometry group at NMSU has already received samples such as strontium titanate/lanthanum aluminate layered structures and Cobalt thin films on $MgAl_2O_4$. Students can use our dielectric function to accurately describe the substrate materials over the entire spectral range. The knowledge gained from performing infrared ellipsometry on the substrate ceramics will allow the group to analyze more complex materials.

APPENDICES

APPENDIX A: DERIVATION OF THE LORENTZ MODEL

Here we show the dielectric function $\epsilon(\omega)$ for a bound charge q under the influence of a time-varying electric field $E(t) = E_0 e^{-i\omega t}$ (e.g. an electromagnetic wave.) We assume the wavelength to be much smaller than the distance between charges and that the amplitude, E_0 is small. We model the effects of the surrounding charges as a velocity-dependent frictional force with a damping coefficient $b = \gamma m$ and the restoring force of the ionic bond as a spring with constant k. This approach is also shown in section 7.5 of Jackson's *Classical Electrodynamics* [51].

The equations of motion for a charge under these conditions can be found from Newton's second law, $F = m\ddot{x}$

$$m\ddot{x}(t) = qE(t) - b\dot{x}(t) - kx(t) \tag{20}$$

Since we know the behavior will be that of a forced and damped harmonic oscillator, we can write the postion $x(t) = x_0 e^{-i\omega t}$.When inserted in Eq. (20), this becomes

$$-m\omega^2 x_0 = qE_0 + ib\omega x_0 - kx_0 \tag{21}$$

where $e^{-i\omega t}$ appears in every term and is canceled. Solving for x_0 gives

$$x_0 = \frac{-qE_0}{m\omega^2 + ib\omega - k} \tag{22}$$

and finally

$$x(t) = \frac{-qE_0}{m\omega^2 + ib\omega - k} e^{-i\omega t} \tag{23}$$

$$\dot{x}(t) = \frac{-qi\omega E_0}{m\omega^2 + ib\omega - k} e^{-i\omega t} \tag{24}$$

$$\ddot{x}(t) = \frac{-q\omega^2 E_0}{m\omega^2 + ib\omega - k} e^{-i\omega t} \tag{25}$$

49

we can write the resonance frequency of the oscillator (without damping) as

$$\omega_0 = \sqrt{\frac{k}{m}} \tag{26}$$

and, recalling that $b = \gamma m$, we can write $x(t)$ including this resonance

$$x(t) = \frac{-qE_0/m}{\omega^2 - \omega_0^2 + i\gamma\omega} e^{-i\omega t} \tag{27}$$

This describes the position of the charge as it is driven by the time-varying field. However, the damping will cause the displacement to lag behind the field. We can find this phase difference ϕ by separating the amplitude of the motion x_0 into real and imaginary parts. The inverse tangent of their ratio gives ϕ [51].

$$x_0 = \frac{-qE_0(m\omega^2 - k)}{(m\omega^2 - k)^2 + b^2\omega^2} + i\frac{-qE_0 b\omega}{(m\omega^2 - k)^2 + b^2\omega^2} \tag{28}$$

$$\tan\phi = -\frac{b\omega}{m\omega^2 - k} = \frac{\gamma\omega}{\omega_0^2 - \omega^2} \tag{29}$$

We see that at the resonance frequency, when $\omega = \omega_0$, $\tan\phi \to \infty$ and the phase difference between displacement and field is $\frac{\pi}{2}$.

We can also use Eq. (??) to determine the complex dielectric function of a material containing n identical bound charges. We recall that

$$\epsilon(\omega) = 1 + \chi(\omega) \tag{30}$$

where $\chi(\omega)$ is the complex dielectric susceptibility. Remebering that the polarization of a material is given by the dipole moment per unit volume and can also be expressed as the susceptibility multiplied by the electric field

$$P(t) = qnx(t) = \epsilon_0\chi(\omega)E(t) \tag{31}$$

from this relationship, we obtain

$$P(t) = -\frac{q^2 n}{m\omega^2 + ib\omega - k} \tag{32}$$

$$\chi(\omega) = -\frac{q^2 n}{\epsilon_0 (m\omega^2 + ib\omega - k)} \tag{33}$$

$$\epsilon(\omega) = 1 + \chi(\omega) = 1 - \frac{q^2 n}{\epsilon_0 (m\omega^2 + ib\omega - k)} \tag{34}$$

To simplify, we define the plasma frequency

$$\omega_p^2 = \frac{q^2 n}{m\epsilon_0} \tag{35}$$

and write the dielectric function in the form used in the Lorentz oscillator model in this work

$$\epsilon(\omega) = 1 - \frac{m\omega_p^2}{m\omega^2 + ib\omega - k} = 1 + \frac{\omega_p^2}{\omega_0^2 - \omega^2 - i\gamma\omega} \tag{36}$$

where ω_0 is the frequency of the phonon and γ is the broadening due to the surrounding charges.

APPENDIX B: PHONON SYMMETRY ANALYSIS

Every crystal belongs to one each of 230 space groups and 32 point groups. These designations define the symmetry of the crystal structure and determine many of its properties. For example, if we know the point group of our crystal, we can use the symmetry to determine the number and activity of its phonons. The phonon calculations for the two materials in this study are given in this appendix.

As an introduction we consider a simple cubic crystal with two atoms such as NaCl. This material has a three-fold degenerate acoustic phonon where the entire two-atom unit shifts out of equilibrium. The point group symmetry tells us that this mode is identical along the x, y, and z axes, hence the degeneracy. In addition to this mode, there is a single optical phonon with the ionic bond stretching and contracting. This too is three-fold degenerate due to the crystal symmetry. Lower symmetry crystals have less degeneracy but may have more overall phonons depending on the number of atoms per unit cell. For a more rigorous explanation, see David Snoke's *Solid State Physics* [52].

Lanthanum Aluminate

Lanthanum aluminate LaAlO$_3$ has a cubic structure above 800 K. At room temperature, it is skewed to a rhobohedral structure which belongs to the space group R$\bar{3}$c and point group D_{3d}^6. The rhombohedral structure has two formula units per unit cell. This gives $N = 10$ atoms and $3N = 30$ degrees of freedom. Three of these are acoustic which leaves 27 possible optical phonon modes.

The D_{3d}^6 point group has the character table

D_{3d}^6	E	$2C_3$	$3C_2'$	i	$2S_6$	$3\sigma_d$
A_{1g}	1	1	1	1	1	1
A_{2g}	1	1	-1	1	1	-1
E_g	2	-1	0	2	-1	0
A_{1u}	1	1	1	-1	-1	-1
A_{2u}	1	1	-1	-1	-1	1
E_u	2	-1	0	-2	1	0

where the column headers define symmetry operations and the rows are the characters of the point group. Some of these characters will not appear as phonons.

E	Identity operation/degeneracy
C_n	$\dfrac{2\pi}{n}$ rotation
i	Inversion
S_n	$\dfrac{2\pi}{n}$ rotation + inversion
σ	Mirror planes

E modes are doubly degenerate while A modes are only singly degenerate. Therefore, a three-fold degenerate mode (T) in the cubic structure will split into one E and one A mode when the symmetry is lowered.

To determine the distribution of these modes, we calculate the character of each symmetry operation g.

$$\chi(g) = N_g \left[\det(g) + 2 \cos \phi \right] \tag{37}$$

where N_g is the number of atoms which are left invariant under the given operation and ϕ is the angle of rotation of the operation. We find N_g using a visualization tool

D_{3d}^6	E	$2C_3$	$3C_2'$	i	$2S_6$	$3\sigma_d$
N_g	10	10	4	2	4	0
La	2	2	2	0	2	0
Al	2	2	2	2	2	0
O_3	6	6	0	0	0	0

Using these values for N_g, we find $\chi(g)$

D_{3d}^6	E	$2C_3$	$3C_2'$	i	$2S_6$	$3\sigma_d$
N_g	10	10	4	2	4	0
$[\det(g) + 2\cos\phi]$	3	0	-1	-3	0	1
$\chi(g)$	30	0	-4	-6	0	0

We then break this character into a unique and irreducible representation using the modes of the point group

D_{3d}^6	E	$2C_3$	$3C_2'$	i	$2S_6$	$3\sigma_d$
$\chi(g)$	30	0	-4	-6	0	0
A_{1g}	1	1	1	1	1	1
A_{2g}	1	1	-1	1	1	-1
E_g	2	-1	0	2	-1	0
A_{1u}	1	1	1	-1	-1	-1
A_{2u}	1	1	-1	-1	-1	1
E_u	2	-1	0	-2	1	0

$$\chi(g) = 1A_{1g} + 3A_{2g} + 4E_g + 2A_{1u} + 4A_{2u} + 6E_u \tag{38}$$

We can see that we have 30 total modes as each E mode is doubly degenerate. Using the selection rules as shown in [52] we can determine the activity of each mode.

$$\text{Acoustic: } 1A_{2u} + 1E_u$$

$$\text{Silent: } 3A_{2g} + 2A_{1u}$$

$$\text{Raman: } 1A_{1g} + 4E_g$$

$$\text{Infrared: } 3A_{2u} + 5E_u$$

The 13 infrared modes are the phonons under investigation in this study.

Spinel

Magnesium aluminate spinel($MgAl_2O_4$) is a cubic crystal and the namesake of the spinel group: $A^{2+}B_2^{3+}O_4^{2-}$. This material has the space group $Fd3m$ and point group O_h^7 and, like LaAlO$_3$, has two formula units per unit cell. This gives $N = 14$ atoms per unit cell and therefore $3N = 42$ possible phonon modes. With three of these being acoustic, we arrive at 39 possible optical modes. All 42 modes and their activities can be derived from the character tables for point group O_h^7

O_h^7	E	$8C_3$	$3C_2$	$6C_4$	$6C_2'$	i	$8S_6$	$3\sigma_h$	$6S_4$	$6\sigma_d$
A_{1g}	1	1	1	1	1	1	1	1	1	1
A_{2g}	1	1	1	-1	-1	1	1	1	-1	-1
E_g	2	-1	2	0	0	2	-1	2	0	0
T_{1g}	3	0	-1	1	-1	3	0	-1	1	-1
T_{2g}	3	0	-1	-1	1	3	0	-1	-1	1
A_{1u}	1	1	1	1	1	-1	-1	-1	-1	-1
A_{2u}	1	1	1	-1	-1	-1	-1	-1	1	1
E_u	2	-1	2	0	0	-2	1	-2	0	0
T_{1u}	3	0	-1	1	-1	-3	0	1	-1	1
T_{2u}	3	0	-1	-1	1	-3	0	1	1	-1

We see that the cubic structure of spinel contains many more symmetry operations as well as the three-fold degenerate T modes which were split in the rhombohedral symmetry of LaAlO$_3$. We can use the same procedure as described for LaAlO$_3$ to find the character of MgAl$_2$O$_4$ with Eq. (37)

O_h^7	E	$8C_3$	$3C_2$	$6C_4$	$6C_2'$	i	$8S_6$	$3\sigma_h$	$6S_4$	$6\sigma_d$
$\chi(g)$	42	0	-2	0	-2	-12	0	0	-2	8

This character can be described with a unique combination of the O_h^7 modes

O_h^7	E	$8C_3$	$3C_2$	$6C_4$	$6C_2'$	i	$8S_6$	$3\sigma_h$	$6S_4$	$6\sigma_d$
$\chi(g)$	42	0	-2	0	-2	-12	0	0	-2	8
A_{1g}	1	1	1	1	1	1	1	1	1	1
A_{2g}	1	1	1	-1	-1	1	1	1	-1	-1
E_g	2	-1	2	0	0	2	-1	2	0	0
T_{1g}	3	0	-1	1	-1	3	0	-1	1	-1
T_{2g}	3	0	-1	-1	1	3	0	-1	-1	1
A_{1u}	1	1	1	1	1	-1	-1	-1	-1	-1
A_{2u}	1	1	1	-1	-1	-1	-1	-1	1	1
E_u	2	-1	2	0	0	-2	1	-2	0	0
T_{1u}	3	0	-1	1	-1	-3	0	1	-1	1
T_{2u}	3	0	-1	-1	1	-3	0	1	1	-1

the irreducible representation gives us

$$\chi(g) = 1A_{1g} + 1E_g + 1T_{1g} + 3T_{2g} + 2A_{2u} + 2E_u + 5T_{1u} + 2T_{2u} \qquad (39)$$

Checking, we have 42 total modes (T=3-fold, E = 2-fold) of which one T_{1u} is acoustic, the A_{1g}, E_g and three T_{2g} are Raman active. The remaining four T_{1u} modes are infrared active and any others are silent. These four modes are visi-

ble as peaks in the imaginary dielectric function as shown in the body of this work.

APPENDIX C: BANDS OF TOTAL REFLECTION

From the fundamental equation of ellipsometry,

$$\frac{r_p}{r_s} = \rho = \tan \Psi * e^{i\Delta}$$

we can see that the complex reflectance ratio, ρ is the ratio of the reflected intensity of p-polarized light, r_p and that of s-polarized light, r_s. An increasingly popular method of infrared ellipsometry data analysis is to look at the frequency regions where $|r_p|^2$ and $|r_s|^2$ are equal to one. That is to say, no light propagates at the given frequency and phonons are therefore forbidden to exist. These bands of total reflection correspond to the reststrahlen bands discussed in the body of this work. Here we calculate the bands of total reflection for $LaAlO_3$ and $MgAl_2O_4$ as a function of incident angle to observe the reststrahlen bands as well as the angular dispersion of the LO phonon modes.

To calculate these bands, we may simply use the experimental data. However, for clarity and to obtain a full angular band, we use the Lowndes model

$$\epsilon(\omega) = \epsilon_\infty \prod_i \frac{\omega_{i,\text{LO}}^2 - \omega^2 - i\gamma_{i,\text{LO}}\omega}{\omega_{i,\text{TO}}^2 - \omega^2 - i\gamma_{i,\text{TO}}\omega}$$

with the broadenings set to zero, calculate the dielectric function and insert it into Eq. (5)

$$\epsilon \approx \langle \epsilon \rangle = \left(\frac{1-\rho}{1+\rho} \right)^2 \tan\phi^2 \sin\phi^2 + \sin\phi^2$$

. We then invert this and calculate $|r_p|^2$ and $|r_s|^2$ as a function of angle ϕ. The results for $LaAlO_3$ are shown in Fig. 15. The regions where $|r_p|^2$ and $|r_s|^2$ are then plotted as a function of angle to obtain the bands of total reflection shown in Fig. 16
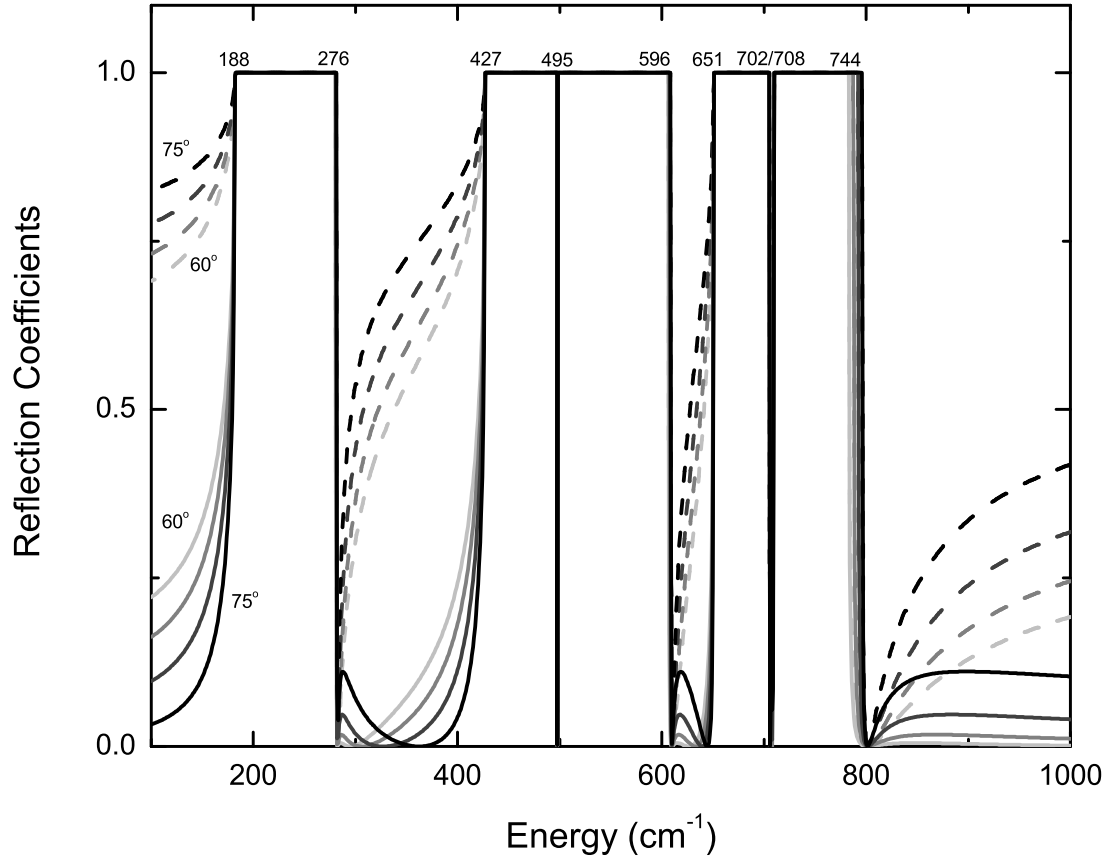
Figure 15: Reflection coefficients for LaAlO$_3$ calculated for four different angles using Eq. (11) with broadenings set to zero. Solid Lines are $|r_p|^2$, dashed indicate $|r_s|^2$.
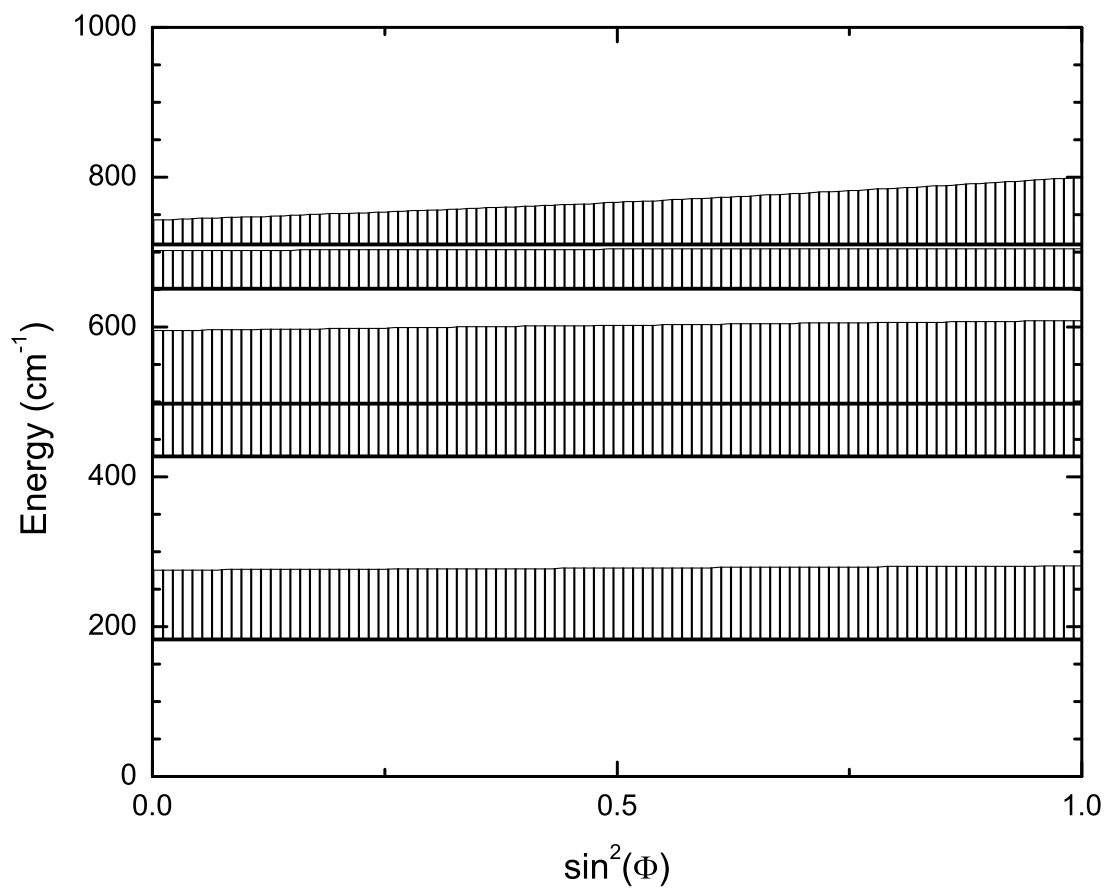
Figure 16: Bands of total reflection for LaAlO$_3$. Reststrahlen bands are hatched with horizontal lines indicating phonon frequencies. Note the increase in angular dispersion at higher energies.

REFERENCES

[1] C.M. Nelson, M. Spies, L.S. Abdallah, S. Zollner, Y. Xu, and H. Luo, J. Vac. Sci. Technol. A **30**, 061404 (2012)

[2] J.A. Woolam Co., Inc., *Guide to Using WVASE32®*, (J.A. Woollam Co., Inc., Lincoln, NE, 2009)

[3] R.M.A. Azzam and N.M. Bashara, *Ellipsometry on Polarized Light,* (North-Holland Publ. Co., Amsterdam, 1984).

[4] F. Gervais and B. Piriou, J. Phys. C Solid State **7**, 2374 (1974).

[5] R.P. Lowndes, Phys. Rev. B **1**, 2754 (1970).

[6] B.J. Gibbons and S. Trolier-McKinstry, IEEE Trans. Appl. Supercon. **7**, 2177 (1997).

[7] A. Ohtomo and H.Y. Hwang, Nature (London) **427**, 423 (2004).

[8] J. Mannhart and D.G. Schlom, Science **327**, 1607 (2010).

[9] J.K. Lee and A.A. Demkov, Phys. Rev. B **78**, 193104 (2008).

[10] S.-G. Lim, S. Kriventsov, T.N. Jackson, J.H. Haeni, D.G. Schlom, A.M. Balbashov, R. Uecker, P. Reiche, J.L. Freeouf, and G. Lucovsky, J. Appl. Phys. **91**, 4500 (2002).

[11] X.-B. Lu, Z.-G. Liu, Y.-P. Wang, Y. Yang, X.-P. Wang, H.-W. Zhou, and B.-Y. Nguyen, J. Appl. Phys. **94**, 1229 (2003).

[12] A.A. Knizhnik, I.M. Iskandarova, A.A. Bagatur'yants, B.V. Potapkin, L.R.C. Fonseca, and A. Korkin, Phys. Rev. B **72**, 235329 (2005).

[13] C. de Rango, G. Tsoucaris, and C. Zelwer, Acta Crystallogr. **20**, 590 (1966).

[14] S.A. Hayward, F.D. Morrison, S.A.T. Redfern, E.K.H. Salje, J.F. Scott, K.S. Knight, S. Tarantino, A.M. Glazer, V. Shuvaeva, P. Daniel, M. Zhang, and M.A. Carpenter, Phys. Rev. B **72**, 054110 (2005).

[15] C.J. Howard, B.J. Kennedy, and B.C. Chakoumakos, J. Phys. - Condens. Mat. **12**, 349 (2000).

[16] X. Luo and B. Wang, J. Appl. Phys. **104**, 073518 (2008).

[17] J.F. Scott, Phys. Rev. **183**, 823 (1969); Phys. Rev. B **1**, 942 (1970) (E).

[18] M.C. Saine, E. Husson, and H. Brusset, Spectrochim. Acta A **37**, 985 (1981).

[19] M.V. Abrashev, A.P. Litvinchuk, M.N. Iliev, R.L. Meng, V.N. Popov, V.G. Ivanov, R.A. Chakalov, and C. Thomsen, Phys. Rev. B **59**, 4146 (1999).

[20] K.A. Müller, W. Berlinger, and F. Waldner, Phys. Rev. Lett. 21, 814 (1968).

[21] P. Delugas, V. Fiorentini, and A. Filipetti, Phys. Rev. B **71**, 134302 (2005). This reference lists incorrect symmetries for the silent modes in Table II, which are corrected in our Table 1.

[22] P. Calvani, M. Capizzi, F. Donato, P. Dore, S. Lupi, P. Maselli, and C.P. Varsamis, Physica C **181**, 289 (1991).

[23] Z.M. Zhang, B.I. Choi, M.I. Flik, and A.C. Anderson, J. Opt. Soc. Am. B **11**, 2252 (1994).

[24] T. Shimada, K. Kakimoto, and H. Ohsato, J. Eur. Ceram. Soc. **25**, 2901 (2005). This reference lists an incorrect space group and therefore also an incorrect factor group. It also misinterprets the experimental implications of the factor group regarding the number of observable phonon modes.

[25] MTI Corporation, Richmond, CA.

[26] J. Humlíček, Philos. Mag. B **70**, 699 (1994).

[27] H.G. Tompkins and W.A. McGahan, *Spectroscopic Ellipsometry and Reflectometry*, (Wiley, New York, 1999).

[28] H. Fujiwara, *Spectroscopic Ellipsometry*, (Wiley, Chichester, UK, 2007).

[29] A.S. Barker, Phys. Rev. **136**, A1290 (1964).

[30] We adopt the notation $\epsilon = \epsilon_1 + i\epsilon_2$, which results from time-period functions of the form $\exp(-i\omega t)$.

[31] D.W. Berreman and F.C. Unterwald, Phys. Rev. **174**, 791 (1968).

[32] T.E. Tiwald, J.A. Woollam, S. Zollner, J. Christensen, R.B. Gregory, T. Wetteroth, S.R. Wilson, and A.R. Powell, Phys. Rev. B **60**, 11464 (1999).

[33] L.F. Edge, D.G. Schlom, P. Sivasubramani, R.M. Wallace, B. Holländer, and J. Schubert, Appl. Phys. Lett. **88**, 112907 (2006).

[34] G. Murtaza and I. Ahmad, J. Appl. Phys. **111**, 123116 (2012).

[35] A. Chopelas and A.M. Hofmeister, Phys. Chem. Minerals **18**, 279 (1991).

[36] J.F. Scott and S.P.S. Porto, Phys. Rev. **161**, 903 (1967).

[37] C.J. Zollner, T. Willett-Gies, S. Zollner and S. Choi, Infrared to vacuum-ultraviolet ellipsometry studies of spinel (MgAl2O4), Thin Solid Films, Available online 15 December 2013, ISSN 0040-6090, http://dx.doi.org/10.1016/j.tsf.2013.11.141.

[38] M. Schubert, T.E. Tiwald, and C.M. Herzinger, Phys. Rev. B **61**, 8187 (2000).

[39] J.X. Ma, D. Mazumdar, G. Kim, H. Sato, N.Z. Bao, and A. Gupta, J. Appl. Phys. **108**, 063917 (2010).

[40] W.L. Rance, A.G. Norman, and A.J. Ptak, J. Crystal Growth, **363**, 40 (2013)

[41] P. Thibaudeau and F. Gervais, J. Phys.: Condens. Matter **14**, 3543 (2002).

[42] S.G. Choi, J. Zúñiga-Pérez, V. Muñoz-Sanjosé, A.G. Norman, C.L. Perkins, and D.H. Levi, J. Vac. Sci. Technology B **28**, 1120 (2010).

[43] W.J. Tropf and M.E. Thomas, in *Handbook of Optical Constants of Solids II*, edited by E.D. Palik, (Academic Press, 1991, San Diego), p. 883.

[44] K. Vedam, J.L. Kirk and B.N.N. Achar, J. Solid State Chem. **12**, 213-218 (1975).

[45] M. Cardona and Sudha Gopalan, in *Progress in Electron Spectroscopy of Solids*, edited by E. Doni, R. Girlanda, G. Pastori Parravicini, and A. Quattropani (Springer, Heidelberg, 1989).

[46] M.L. Bortz, R.H. French, D.J. Jones, R.V. Kasowski, and F.S. Ohuchi, Phys. Scripta **41**, 537 (1990).

[47] R.D. Shannon and G.R. Rossman, J. Phys. Chem. Solids **52**, 1055 (1991).

[48] P.Y. Yu and M. Cardona, *Fundamentals of Semiconductors*, (Springer, Berlin, 1996).

[49] T. Willett-Gies, E. DeLong, and S. Zollner, Vibrational properties of bulk LaAlO$_3$ from Fourier-transform infrared ellipsometry, Thin Solid Films, Available online 14 December 2013, ISSN 0040-6090, http://dx.doi.org/10.1016/j.tsf.2013.11.140.

[50] M. Lazzeri and P. Thibaudeau, Phys. Rev. B **74**, 140301 (R) (2006).

[51] J.D. Jackson, *Classical Electrodynamics,* (Wiley, New York, NY, 3rd edition, 1999).

[52] D. Snoke, *Solid State Physics,* (Addison-Wesley, San Francisco, CA, 2000).